

# Building galaxies by accretion and in-situ star formation

C. N. Lackner<sup>1\*</sup>, R. Cen<sup>1</sup>, J. P. Ostriker<sup>1</sup>, and M. R. Joung<sup>2,3</sup>

<sup>1</sup>*Department of Astrophysical Sciences, Princeton University, Princeton, NJ 08544*

<sup>2</sup>*Department of Astronomy, Columbia University, 550 West 120th Street, New York, NY 10027*

<sup>3</sup>*Department of Astrophysics, American Museum of Natural History, 79th Street at Central Park West, New York, NY 10024*

20 February 2022

## ABSTRACT

We examine galaxy formation in a cosmological AMR simulation, which includes two high resolution boxes, one centered on a  $3 \times 10^{14} M_{\odot}$  cluster, and one centered on a void. We examine the evolution of 611 massive ( $M_* > 10^{10} M_{\odot}$ ) galaxies. We find that the fraction of the final stellar mass which is accreted from other galaxies is between 15 and 40% and increases with stellar mass. The accreted fraction does not depend strongly on environment at a given stellar mass, but the galaxies in groups and cluster environments are older and underwent mergers earlier than galaxies in lower density environments. On average, the accreted stars are  $\sim 2.5$  Gyrs older, and  $\sim 0.15$  dex more metal poor than the stars formed in-situ. Accreted stellar material typically lies on the outskirts of galaxies; the average half-light radius of the accreted stars is 2.6 times larger than that of the in-situ stars. This leads to radial gradients in age and metallicity for massive galaxies, in qualitative agreement with observations. Massive galaxies grow by mergers at a rate of approximately  $2.6\%/Gyr^{-1}$ . These mergers have a median (mass-weighted) mass ratio less than  $0.26 \pm 0.21$ , with an absolute lower limit of 0.20, for galaxies with  $M_* \sim 10^{12} M_{\odot}$ . This suggests that major mergers do not dominate in the accretion history of massive galaxies. All of these results agree qualitatively with results from SPH simulations by Oser et al. (2010, 2012).

**Key words:** galaxies: evolution galaxies: formation methods: numerical

## 1 INTRODUCTION

In a  $\Lambda$ CDM cosmology, galaxy growth is hierarchical; large galaxies form by accreting smaller systems of gas, stars, and dark matter. This model has been extensively tested by simulations and observations. However, it is not known whether stars or gas dominate the accretion history of galaxies, and what effects this accretion has on the observable properties of the galaxies. With modern hydrodynamical simulations, we can directly measure what fraction of the stars in a massive galaxy have been formed in-situ and what fraction have been made in other galaxies which were subsequently accreted by the parent galaxy. Similarly, we can map out when accretion occurs, what kind of accretion events dominate, and how the accretion affects the observable properties of galaxies. In this work, we explore these effects for a set of massive galaxies from a hydrodynamical cosmological simulation.

Oser et al. (2010) (hereafter Os10) present a useful framework for studying the hierarchical build-up of galaxies. Based on hydrodynamical simulations of early-type galaxy formation, they suggest that massive galaxy forma-

tion can be divided into two phases: an early, rapid in-situ star formation period followed by a late merger-dominated period. The former period is similar to the picture previously called “monolithic collapse” (Eggen et al. 1962; Larson 1975; Carlberg 1984) and currently labelled “cold flow-driven” star formation (e.g. Dekel & Birnboim 2006; Dekel et al. 2009; Elmegreen et al. 2009; Ceverino et al. 2010), while the latter phase is similar to prior pictures of galactic cannibalism (Ostriker & Hausman 1977; White & Rees 1978; Searle & Zinn 1978; Kauffmann et al. 1993). In this scheme, individual stars can be classified according to whether they formed within the virial radius of the final system (in-situ) or outside of it (accreted). Os10 show that this distinction between stars is unambiguous; there is a large spatial separation between the birth places of stars formed in-situ and those added in accretion events. They further show that massive galaxies are dominated by accreted stars, which are typically older than stars formed in-situ. In this work, we find that the accreted stars in a galaxy are older, more metal-poor, and found at larger radii in the final galaxy than stars formed in-situ. The metallicity trends are consistent with observations of radial trends in colour (e.g. de Vaucouleurs 1961; Tortora et al. 2010; Tal & van Dokkum 2011), metallicity

\* E-mail: clackner@astro.princeton.edu

(Spinrad & Taylor 1971; Faber et al. 1977; Davies et al. 1993; Brough et al. 2007; Rawle et al. 2008; Spolaor et al. 2010; Kuntschner et al. 2010; Coccato et al. 2011) and globular cluster metallicities (Forbes et al. 2011; Arnold et al. 2011) in early-type galaxies.

The differences between accreted and in-situ stars are also seen in disc galaxies. For example, in the Milky Way stellar halo, there has long been observational evidence for at least two stellar populations. The inner halo consists of stars with high  $\alpha$ -element abundances (e.g. Nissen & Schuster 2010) and rotates with the galactic disk (Deason et al. 2011), while the outer halo has low  $\alpha$ -element abundances and is not rotating, suggesting it was created by accretion of satellite galaxies. Simulations of disc galaxies show that the differences in dynamics and chemical abundances in the stellar halo are due to the differences in the accreted and in-situ stellar populations (Brook et al. 2004; Abadi et al. 2006; Zolotov et al. 2009, 2010; Font et al. 2011).

The two phase model of galaxy formation (i.e., early, in-situ star formation and late accretion) is also useful in explaining the evolution of compact, massive ellipticals at  $z \sim 2$  (Trujillo et al. 2007; van Dokkum et al. 2008; Damjanov et al. 2009; van Dokkum & Brammer 2010; Oser et al. 2012). Both direct profile measurements and velocity dispersions have shown that these systems are  $\sim 100$  times denser (within 1 effective radius) than present-day ellipticals of the same mass (Daddi et al. 2005; van Dokkum et al. 2008; van der Wel et al. 2008, 2011; van de Sande et al. 2011). However, if compared on same *physical* scale, the densities in the central portions of  $z \approx 2$  and present-day ellipticals are similar, suggesting that early-type galaxies have increased their size through minor, dry mergers which add stars to the outskirts of massive galaxies (Naab et al. 2007, 2009; Bezanson et al. 2009; Hopkins et al. 2009; Carrasco et al. 2010; Oser et al. 2012; Tal et al. 2012, but see Newman et al. 2012). By using close companions to estimate the merger rate of compact galaxies at  $0.4 < z < 2.5$ , Newman et al. (2012) observe that minor merging may not be sufficient to explain the size evolution of compact galaxies from  $z \approx 2$ . However, the size evolution due to minor mergers has been found in hydrodynamical simulations (e.g. Naab et al. 2009; Oser et al. 2012) and is consistent with the size growth found by observations.

In this work, we make use of galaxy catalogs from cosmological simulations done with adaptive mesh refinement (AMR) (Cen 2012). The use of an Eulerian grid-based code instead of a Lagrangian particle-based code is a notable distinction between this work and that of Os10. Scannapieco et al. (2011) find that different numerical hydrodynamics can yield differences of a factor of two in simulated galaxy properties. However, Scannapieco et al. (2011) find that changes in the feedback implementation can yield even larger differences in the simulation results. We will address the differences in sub-grid physics between our work and that of Os10 below. The AMR simulation studied here contains two high resolution boxes, one centered on a galaxy cluster and another centered on a void. These large volumes simulated at high resolutions allow us to study the merging histories of more than 600 galaxies in a variety of environments, from void to group to cluster. Following Os10, we have divided the stars in each galaxy into accreted and in-situ, which allows us to examine the star formation his-

tories for the galaxies as a function of stellar mass and environment. The qualitative similarities between our results and those of Os10, despite profound differences in numerical techniques and sub-grid physics, help substantiate the two-phase model of galaxy evolution for early type galaxies.

The paper is divided into the following sections: §2 details the simulation, the building of the merging histories and the tagging of stars as accreted or in-situ; §3 and §3.1 describe the properties of the in-situ and accreted stars and compare our simulation results to those of Os10. §4 focuses on the merger histories and the types (major vs. minor) of mergers the galaxies in our simulation underwent and their effects on the final galaxy properties. For the simulation and throughout this work, we use the following  $\Lambda$ CDM cosmology, consistent with WMAP-7 (Komatsu et al. 2011):  $\Omega_M = 0.28$ ,  $\Omega_\lambda = 0.72$ ,  $\Omega_b = 0.046$ ,  $\sigma_8 = 0.82$ ,  $n = 92$ ,  $H_0 = 100h \text{ km s}^{-1} \text{ Mpc}^{-1}$ , and  $h = 0.7$ .

## 2 DESCRIPTION OF SIMULATION

This work uses the same cosmological simulations as Cen (2012, 2011b), and further descriptions of the methodology can be found there. The simulations are performed with the AMR Eulerian hydrodynamics code, Enzo (Bryan 1999; O’Shea et al. 2004; Joung et al. 2009). Enzo uses the particle-mesh technique for the dark matter N-body dynamics. Poisson’s equation is solved using a fast-Fourier transform on the base grid and multigrid relaxation on the higher resolution subgrids (O’Shea et al. 2004). Enzo solves the hydrodynamics using a modified version of the piecewise parabolic method (Woodward & Colella 1984; O’Shea et al. 2004), which is formally second-order accurate and conserves energy, momentum and mass fluxes. For this work, two regions, a cluster and a void, were selected from a low resolution simulation of a periodic box  $120 h^{-1} \text{ Mpc}$  on a side. These regions were re-simulated separately at high resolution. The cluster box is  $21 \times 24 \times 20 h^{-3} \text{ Mpc}^3$ , and the void box is  $31 \times 31 \times 35 h^{-3} \text{ Mpc}^3$ . These regions represent  $+1.8\sigma$  and  $-1.0\sigma$  fluctuations, respectively. The refined regions are surrounded by two buffer layers,  $\sim 1 h^{-1} \text{ Mpc}$  thick, which connect to the underlying low-resolution periodic simulation box of  $120 h^{-1} \text{ Mpc}$ . The resolution in the refined regions is  $460 h^{-1} \text{ pc}$  physical or better. The two refined regions are similar to two of the five regions taken from the Millennium Simulation (Springel et al. 2005) and then simulated at high resolution in Crain et al. (2009). The volume of the void box used here is 5 times larger than the regions simulated in Crain et al. (2009), while the cluster box is comparable in size to the  $+2\sigma$  region in Crain et al. (2009).

In the refined regions, the dark matter particle mass is  $1.07 \times 10^8 M_\odot$ , and the stellar particle mass is typically  $10^6 M_\odot$ . Each stellar particle is tagged with its initial mass, metallicity, dynamical time, and formation time. Additionally, the luminosity of each star particle in the five Sloan Digital Sky Survey (SDSS) filters (Fukugita et al. 1996) is computed using the Galaxy Isochrone Synthesis Spectral Evolution Library (GISSEL) stellar synthesis code (Bruzual & Charlot 2003), assuming a Salpeter initial mass function (IMF).

The simulations include a UV background (Haardt & Madau 1996), a prescription for shielding

from UV by neutral hydrogen (Cen et al. 2005), and metallicity dependent radiative cooling (Cen et al. 1995). The UV background radiation field is subject to self-shielding; we compute the local ionization and cooling/heating balance for each cell in the following way. A local optical depth approximation is adopted to crudely mimic the local shielding effects: each cubic cell is flagged with six hydrogen “optical depths” on the six faces, each equal to the product of the neutral hydrogen density, hydrogen ionization cross section and scale height. The appropriate mean from the six values is then calculated. Equivalent means for neutral helium and singly-ionized helium are also computed. Metal cooling is computed with ionization equilibrium including the effects of the redshift-dependent UV-X-ray background, using a code based on the standard Raymond-Smith code (Raymond et al. 1976). The cosmological reionization in this model occurs at redshift  $z = 8 - 9$ .

Star particles are created in cells that satisfy the criteria set forth in Cen & Ostriker (1992). Specifically, stars are created when the baryon overdensity,  $\delta\rho_b/\rho > 5.5$  and the following are true:

$$\nabla \cdot \mathbf{v} < 0 \quad , \quad (1a)$$

$$t_{\text{cool}} < t_{\text{dyn}} \equiv \sqrt{\frac{3\pi}{32G\rho_{\text{tot}}}} \quad , \text{ and} \quad (1b)$$

$$m_b > m_{\text{Jeans}} \equiv \frac{c_s^3}{G^{3/2}\rho_b^{1/2}(1 + \rho_b/\rho_d)^{3/2}} \quad , \quad (1c)$$

where  $c_s$  is the sound speed and  $\rho_b$  and  $\rho_d$  are the baryon and dark matter densities, respectively.

Supernovae feedback is modeled as in Cen et al. (2005). Feedback thermal energy and metal-enriched ejecta is distributed into the 27 cells surrounding the star particle. The amount added to each cell is inversely proportional to the density of each cell, mimicking the process of supernovae blast waves, which channel energy into the least dense surrounding regions. The rate of feedback has the form  $1/t_{\text{dyn}} [(t - t_i)/t_{\text{dyn}}] \exp[-(t - t_i)/t_{\text{dyn}}]$ , where  $t_i$  is the formation time of a given star particle, and  $t_{\text{dyn}}$  the dynamical time of the cell. Accounting for both Type II and prompt Type I supernovae, the total amount explosion kinetic energy per stellar mass ( $M_*$ ) formed (assuming a Chabrier IMF) is  $\epsilon_{\text{SN}} M_* c^2$ , where  $\epsilon_{\text{SN}} = 1 \times 10^{-5}$ . The feedback process is entirely hydrodynamically coupled to the surroundings and subject to all physical processes, such as cooling. The simulations do not include input from active galactic nuclei; its absence may contribute to the excess of massive galaxies.

Several tests of the feedback process for these simulations are presented in earlier works. Cen (2012) show that the kinematic properties of damped Lyman-alpha systems in the simulations agree well with observations, providing a significant test to the feedback model. In Cen (2011b) we show that the phenomenon of cosmic downsizing can be naturally explained in our model with the necessary large-volume cosmological setting, due to correlations between galaxy environment and astrophysical processes that operate on gas physics. In Cen (2011c) we show that galaxy luminosity functions for both UV and FIR selected galaxies can be self-consistently produced by the simulation, when reprocessing of optical-UV radiation into IR radiation is followed in detail. In Cen (2011a), we show that our model reproduces

a variety of observed properties of O VI  $\lambda\lambda 1032, 1038$  absorption lines at  $z \sim 0$ . In combination, these tests strongly indicate a range of applicability of our simulations to complex systems, from galaxies at kpc scales to Mpc scales in the intergalactic medium, and empirically validate our star formation feedback prescription, upon which all these phenomena critically depend. This validation of the simulation results is critical and allows us, with significant confidence, to perform the particular analysis presented here.

## 2.1 Merger trees

In order to identify galaxies in a given snapshot, we use the HOP algorithm on stellar particles (Eisenstein & Hu 1999; Cen 2011b). For the HOP program we choose an outer stellar overdensity of  $\delta_{\text{outer}} = 10000$ , and density ratios of  $\delta_{\text{saddle}} = 2.5\delta_{\text{outer}}$  and  $\delta_{\text{peak}} = 3\delta_{\text{outer}}$ ; these ratios are recommended by Eisenstein & Hu (1999). We have examined 600 groupings with  $M_* > 5 \times 10^9 M_\odot$  at  $z = 0$  in the cluster simulation and have found 9 HOP groupings which contain more than one (usually two) visually distinguishable galaxies. The central galaxy of the cluster is included in one such grouping. We find no such groupings in the void box. This represents a contamination of  $\lesssim 2\%$  of our galaxy sample. For the remainder of the paper, we will exclude the 9 groupings which have not been adequately separated by the HOP algorithm at  $z = 0$ .

In order to study the accretion histories of the galaxies, we build merger trees for the simulations. For the cluster box, we use 38 snapshots: one every  $\Delta z = 0.05$  between  $z = 0$  and 1.35. Beyond  $z = 1.35$ , we have snapshots at  $z = 1.5, 1.6, 1.75, 1.9, 2.0, 2.2, 2.5, 2.8, 3.1$ , and 4. For the void box, we only use 14 redshift slices at  $z = 0, 0.05, 0.15, 0.2, 0.4, 0.5, 0.6, 0.8, 1.0, 1.6, 1.9, 2.5, 3.1$  and 4. The merger trees are built by looking at the overlap of the stellar particles in galaxies in sequential redshift slices. For example, if most of the stars in galaxy B at  $z = 0.05$  are later in galaxy A at  $z = 0$ , we label galaxy B a parent of galaxy A. Galaxy A may have many parents at  $z = 0.05$ ; we call the main progenitor (the same galaxy at an earlier time) the galaxy that contributes the most mass to the child galaxy. The remainder of the parent galaxies are galaxies which have merged into the main galaxy during the current redshift step. This process can be repeated for all the galaxies in all the redshift slices. Each galaxy has a progenitor and possibly a set of galaxies which have just merged into it. Stepping back through the main progenitors gives a full history for a given galaxy.

We verify this method of grouping by using every other redshift slice and checking that the progenitors do not change. Ninety-two percent (91%) of the galaxy merger trees in the cluster (void) box are the same to  $z = 1$  if we only use every other redshift slice. The galaxies with modified histories are typically below our mass threshold. We also check that the 200 most-central particles in a galaxy have significant overlap with the 200 most-central particles in its main progenitor. This is true for more than 98% of the galaxies with masses above  $5 \times 10^9$  for the cluster box and 95% of the galaxies in the void box. The majority of galaxies which fail this test cannot be traced back to  $z > 2.0$  and will not be used in our analysis.

After identifying merger histories for each galaxy, we

can label the stars in every  $z = 0$  galaxy as accreted or in-situ. As above, we proceed in a stepwise manner toward high redshift snapshots. For each stellar particle in a galaxy at a given redshift, we examine where it was in the previous redshift slices. Star particles which were in the main progenitor galaxy are labelled as in-situ. Stellar particles in any of the other parent galaxies are labelled as accreted, and the accretion redshift is noted. The remainder of stellar particles were either formed during the current redshift step, and labeled as in-situ, or they formed earlier and are labeled as accreted. These stellar particles are due to accretion from unresolved galaxies, as well as uncertainty in the grouping algorithm. If a star particle was born in the main progenitor galaxy, but later re-accreted, we consider it an in-situ star particle. Such particles contribute between 2 and 5 per cent to the total galaxy stellar mass. We then examine the stars of the main progenitor (those which were initially labeled in-situ) in the same way and repeat the process for all higher redshift slices. This allows us to distinguish between accreted and in-situ stellar material to our highest redshift snapshot at  $z = 4$ .

One difficulty in this method is ensuring that none of the stars we consider in-situ were actually formed outside the galaxy and accreted between snapshots. Os10 find a large separation in space (3 orders of magnitude in distance from the centre of the main progenitor galaxy) between in-situ and accreted particles. However, their Figure 7 also shows the birth places of a population of accreted stars which formed between  $0.1 r_{\text{virial}}$  and  $1.0 r_{\text{virial}}$ . If our redshift snapshots are not sufficiently close together, we will count these stellar particles as in-situ, instead of accreted. We have compared the dynamical time of a virialized halo ( $t_{\text{dyn}} \sim 1/\sqrt{G 200\rho_{\text{crit}}} \sim 1/(10H(z))$ ), to the time between redshift slices. For the cluster, the dynamical time of the halo is larger than the time between redshift slices by at least a factor of 2 for  $z \leq 1.35$ . Beyond  $z = 1.35$ , the halo dynamical time is comparable to the density of redshift snapshots. Therefore, our calculations of the accreted fraction may not include stars formed during infall to the final galaxy, and should be considered lower limits.

## 2.2 Galaxy population

Before examining the merger histories of the simulated galaxies, we have examined the overall properties of the galaxies at  $z = 0$ . Cen (2011b) have shown that the luminosity function for galaxies in the cluster and void agree well with SDSS observations (Blanton et al. 2003), except at the highest luminosities, where the simulation produces too many luminous galaxies. This is due to insufficient feedback; the simulations do not include AGN feedback or stellar feedback from Type I supernovae. Additionally, the highest mass galaxies suffer from overmerging (White 1976; Moore et al. 1996). These highest luminosity bins can be corrected by taking into account AGN feedback and decreasing the stellar mass by a factor of  $1/(1 + (M_{\text{halo}}/1 \times 10^{13} \text{ M}_{\odot})^{2/3})$  (Cen 2011b; Croton et al. 2006).

Figure 1 shows the uncorrected mass function of galaxies in each region at  $z = 0$ , compared to the mass function of SDSS galaxies (Li & White 2009). We have only included galaxies with at least 100 dark matter particles ( $M_{\text{halo}} \gtrsim 10^{10} \text{ M}_{\odot}$ ). The *average* mass function for the simu-

lation is a weighted sum of the cluster and void box. Using the same simulations, Cen (2011b) suggest a weighting of 6 : 1 for the void and cluster box, based on matching the simulated star formation rate history to observations. The weighting scheme of Crain et al. (2009), yields a weighting of 2 : 3 for the void and cluster box, since the cluster box is 63% smaller than the void box, but it's also a rarer density perturbation. For the remainder of this work, we weight the galaxies in the void and cluster box equally, unless otherwise noted.

There is a clear deficit of galaxies with masses below  $\sim 3 \times 10^{10} \text{ M}_{\odot}$ . In fact, if we include galaxies with fewer dark matter particles, both mass functions turn up again and have second low mass peaks at  $M_{*} \sim 10^8 \text{ M}_{\odot}$ , however, these groupings are most likely due to resolution effects. The simulated mass functions bracket the observations well in the range  $10.5 \lesssim \log M_{*}/\text{M}_{\odot} \lesssim 11$ , but as explained above, the simulation overproduces massive galaxies. The overproduction of massive galaxies is a typical problem for hydrodynamical simulations and is due to insufficient feedback to suppress star formation and to overmerging among close pairs of galaxies. This is a serious limitation of our work, and the numerical values we derive from the simulations will certainly change with higher resolution, improved feedback models, and lower star formation rates.

Since improved feedback will reduce the stellar masses of all massive galaxies, it is not obvious if it will decrease number of accreted or in-situ stars more. The high levels of star formation at  $z = 0$  (see §3.1) suggests that most of the excess stars are formed in-situ, but only improved simulations will give a definitive answer. Nonetheless, we are confident in our results for two main reasons. The first is that the differences between accreted and in-situ stars do not depend strongly on mass (see Figures 5–7), and are present even in the lowest mass bin where the mass function of galaxies is reasonable. Secondly, although improved feedback will certainly modify the mass function, it will not substantially alter the rank-ordering of galaxies; the most massive galaxies in our simulation will still be the most massive. Therefore, we expect that trends with stellar mass will have different slopes, but the sign of those slopes should be insensitive to the feedback model. In the next sections, we will only examine the properties of galaxies with at least 100 dark matter particles and stellar masses larger than  $3 \times 10^{10} \text{ M}_{\odot}$ , but we continue to include the most massive galaxies despite their overabundance.

### 2.2.1 Galaxy formation efficiency

Simulations from cosmological initial conditions are known to overproduce stars (Oser et al. 2010; Guo et al. 2010, and references therein). This is true for the simulations in this work as well, and can be easily shown by comparing the mass ratio of dark matter and stars to observations. The ratios of stellar mass to dark matter mass at  $z = 0$  are  $1.2 \times 10^{-2}$  and  $6.0 \times 10^{-2}$  for the void and cluster boxes, respectively. The two weighting schemes discussed above give an average ratio in the range 1.9 to  $4.1 \times 10^{-2}$  for the entire simulation. The observed ratio in the local universe is  $(1.2 \pm 0.3) \times 10^{-2}$  (e.g. Fukugita & Peebles 2004; Gallazzi et al. 2008). The void box has a star formation efficiency which agrees well with the observed average. However, observations show

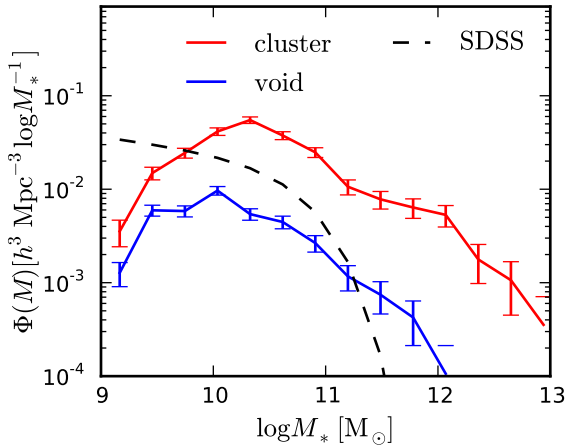


**Figure 1.** The  $z = 0$  mass function of the cluster and void box shown in red and blue, respectively. The mass function from SDSS is shown by the black dashed line (Li & White 2009). The mass functions of the simulated boxed bracket the observations for  $10^{10} M_{\odot} < M_* < 10^{11} M_{\odot}$ . The simulations overproduce galaxies more massive than  $10^{11} M_{\odot}$ .

that underdensities in the universe are also under-luminous (Peebles 2001). Therefore, if the star formation and feedback in the simulation were accurate, the void box would have a lower star to dark matter ratio than the average. Thus, stars are overproduced in both the cluster and the void box, with the overall star formation rate too high by a factor of two to four.

We can examine the overproduction of stars in the cluster box in more detail by computing the ratio  $f_* = M_*/M_{\text{DM}} \times (\Omega_{\text{DM}}/\Omega_b)$  for both simulated and observed galaxies and their host dark matter halos. In the simulations used here, the central cluster has a virial radius (using the radius inside which  $\langle \rho \rangle = 200\rho_{\text{crit}}$ ) of  $1.3 h^{-1} \text{Mpc}$ . The total dark matter mass interior to this radius is  $3.0 \times 10^{14} M_{\odot}$ , and the total stellar mass interior to this radius is  $3.0 \times 10^{13} M_{\odot}$ . Therefore, the efficiency of star formation in the cluster is  $f_* = 0.60$ , or 60% of the baryons in the cluster have been turned into stars by  $z = 0$ . For a cluster of this mass, the expected star formation efficiency from weak lensing and halo occupation distribution (HOD) methods is  $10\% \lesssim f_* \lesssim 15\%$  (Leauthaud et al. 2012). This range is slightly above the values found by matching simulated DM halos to the observed galaxy mass functions (Guo et al. 2010; Behroozi et al. 2010; Moster et al. 2010). Thus, the star formation in the cluster is over-efficient by roughly a factor of four. The simulation star formation efficiency is in part too high due to the lack of sufficient feedback from supernovae and AGN. If we correct the stellar masses to take this into account, as in the previous section, the efficiency decreases to  $\sim 30\%$ .

### 2.2.2 Mean stellar properties

The top panel in Figure 2 shows the relation between galaxy stellar mass and SDSS  $r$ -band luminosity-weighted age. The simulated trend is compared the observed mass-age relation from SDSS (thick gray line) (Gallazzi et al.

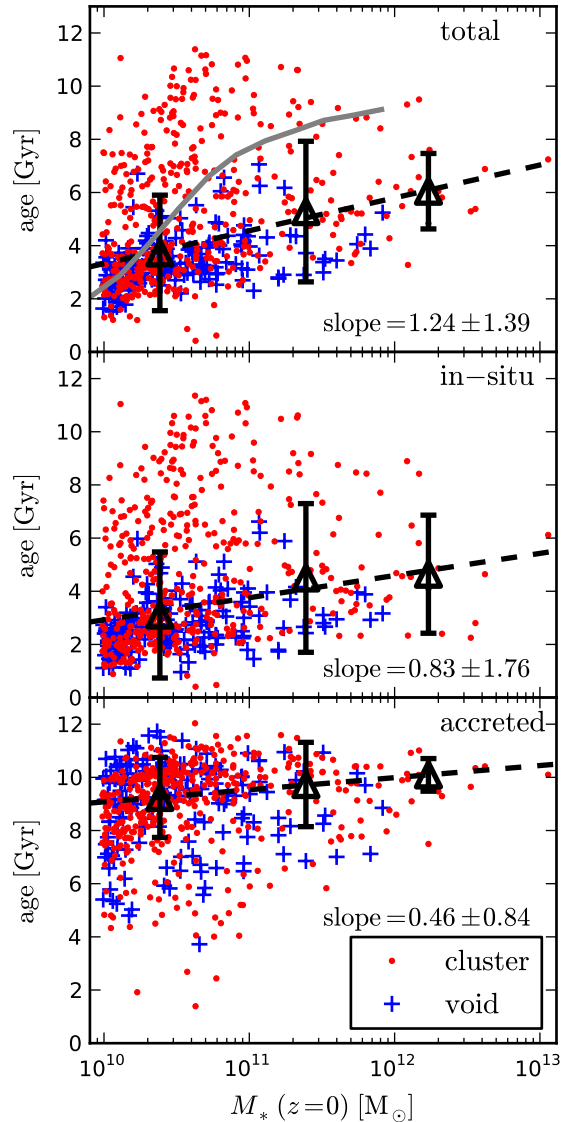


**Figure 2.** The mean (luminosity-weighted) stellar ages for all the stars (top), and the in-situ (middle) and accreted (bottom) stars as a function of total galaxy stellar mass. The large black triangles are the medians and inter-quartile ranges in 3 mass bins. The dashed line is fit the medians. The gray solid line in the top panel is the median observed mass-age relation from SDSS (Gallazzi et al. 2005). The galaxies in the simulation are young compared to observed galaxies. Nonetheless, the accreted stars are uniformly older than the in-situ stars.

2005). Although there is little trend with mass, the youngest galaxies are among the least massive. The lack of trend at high masses is consistent with observations from SDSS (Gallazzi et al. 2005), in which the steepest portion of the stellar mass-stellar age trend occurs in the mass range  $3 \times 10^9 \lesssim M_* \lesssim 3 \times 10^{10}$ . However, the median ages for the galaxies in our sample are several Gyrs younger than observed galaxy ages (Gallazzi et al. 2005). This is partially due to an excess of star formation at late times (see Figure 5) which is related to the insufficient resolution and feedback modeling in the simulation. Figure 2 also shows that the median age of galaxies is dependent on environment, with the

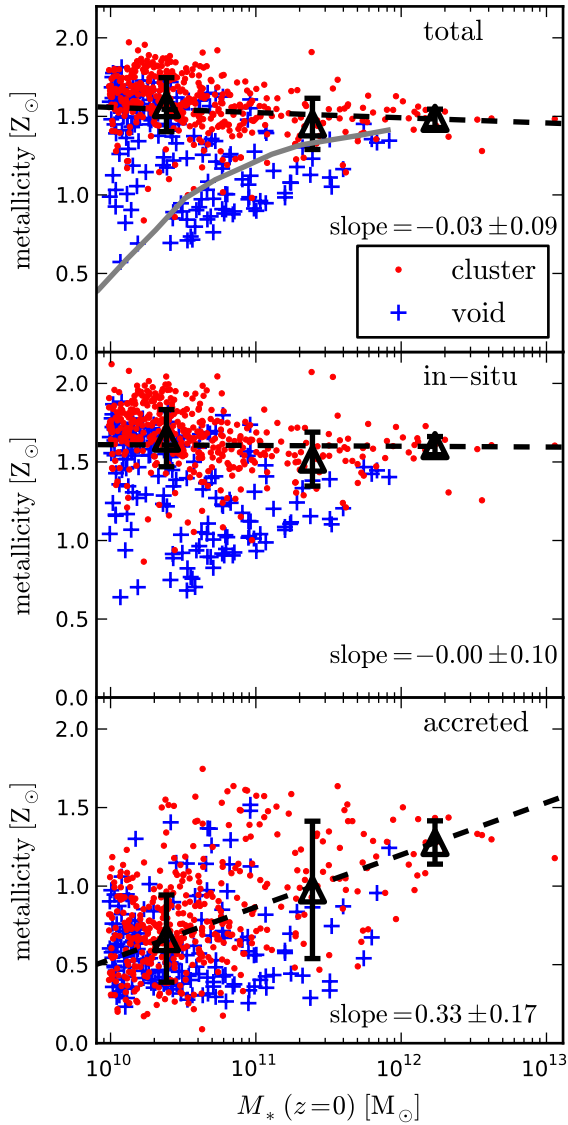


**Figure 3.** The mean (luminosity-weighted) stellar metallicities for all the stars (top), and the stars divided into in-situ (middle) and accreted (bottom) stars as a function of total galaxy stellar mass. The large black triangles are the medians and inter-quartile ranges in 3 mass bins. The dashed line is fit the medians. The gray solid line in the top panel is the median observed mass-metallicity relation from SDSS (Gallazzi et al. 2005). The galaxies in the simulation show no mass metallicity relation, although the maximum metallicity is consistent with observations. The symbols are as in Figure 2.

oldest galaxies found in the cluster box, while none of the void box galaxies are older than  $\sim 7$  Gyr. Thus the trends of galaxy age with stellar mass and local density are broadly consistent with the observational picture of downsizing and the quenching of star formation in cluster environments (see Cen 2011b, for a study of downsizing in this simulation).

It is expected that the trends in metallicity will be similar to those for stellar ages. As with the stellar ages, we find that stellar mass and stellar metallicity are not strongly correlated in the simulations (see Figure 3, top panel). There is a stronger dependence on metallicity with environment; the

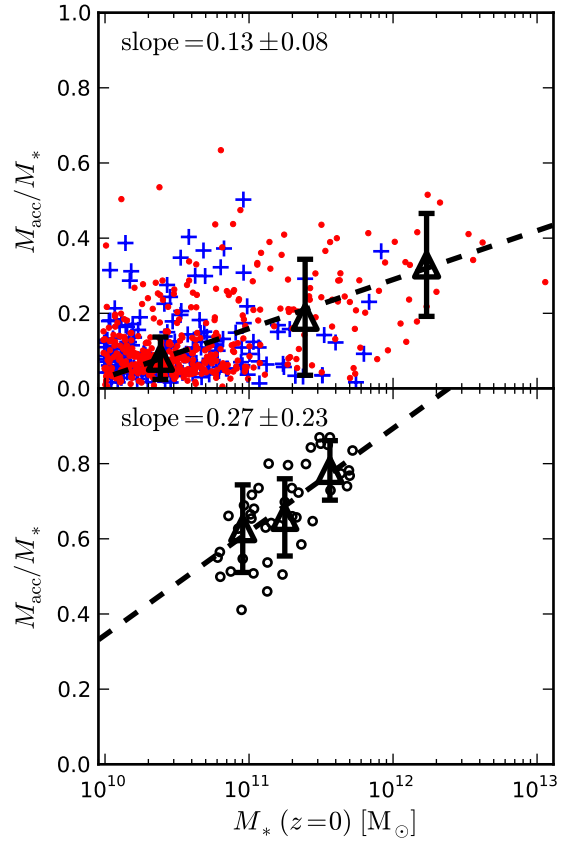


**Figure 4.** The fraction of accreted material ( $M_{acc}/M_*$ ) as a function of final ( $z = 0$ ) stellar mass. In the top panel, the blue(red) points are for the void(cluster) box. The large black triangles are the medians and inter-quartile ranges in 3 mass bins. The line is fit through the medians. The lower panel shows the same for the galaxies simulated in Os10 (data from L. Oser). The accreted fraction found in this work is significantly smaller than that in Os10 for very massive galaxies.

void box galaxies have metallicities around  $Z \approx 1 Z_\odot$ , while the cluster galaxy metallicities are centered at  $Z \approx 1.5 Z_\odot$  with very little scatter. This value of metallicity is consistent with the median metallicity for the most massive ( $M \gtrsim 10^{11} M_\odot$ ) nearby SDSS galaxies (Gallazzi et al. 2005) (grey solid line).

The excess of young stars and overabundance of metals suggests again that the simulations suffer from over-cooling and insufficient feedback. Wiersma et al. (2011) find that changes in the feedback prescription can alter the stellar metallicity by factors of 4. Their simulations suggest that the inclusion of AGN feedback and momentum-driven supernovae winds can bring the stellar metallicity into agreement with observations.

### 3 IN-SITU VS. ACCRETED STARS

In order to examine the accretion history of galaxies, we restrict our sample to galaxies with robust merger histories. We require that galaxies have a stellar mass  $M_* > 10^{10} M_\odot$ , and at least 100 dark matter particles. We also require either that a galaxy can be traced back to  $z > 2.0$  or that its small-

est progenitor of the galaxy has a stellar mass  $M_* < 10^9 M_\odot$ . This removes galaxies which have gaps in their merger history, but retains galaxies which have grown significantly since  $z = 2$ . The sample includes 443 galaxies from the cluster box and 168 galaxies from the void box. These represent  $\sim 85\%$  of the  $z = 0$  galaxies which satisfy the stellar and dark matter mass constraints. We test that this smaller sample is not a biased subset of the larger sample using the Kolmogorov–Smirnov (KS) test. We find the probabilities that the distributions of stellar mass, stellar age, and accreted fraction are the same for both samples are 1.00, 0.99, and 0.98, respectively.

The top panel in Figure 4 shows the fraction of the final stellar mass which was accreted as a function of stellar mass. This figure (and all subsequent figures) only include galaxies for which we have robust merger histories. We find that the accreted fraction increases as a function of stellar mass from  $17 \pm 7\%$  for  $10^{10} \lesssim M_* \lesssim 10^{11} M_\odot$  to  $\sim 40 \pm 15\%$  for the most massive galaxies in the cluster box ( $M_* \gtrsim 10^{12} M_\odot$ ). This value is in agreement with estimates of the merged stellar mass for massive cluster galaxies from observations of paired galaxies (Lin et al. 2010). Although the sign of this trend is consistent with that found in Os10, both the slope and the zero-point are significantly smaller in our sample. The causes of this discrepancy will be discussed further in §3.1. We find no trend with the dynamical age of system and the accreted fraction, in contrast to the results of Font et al. (2011) and Zolotov et al. (2009). The excess of late in-situ star formation in our simulation may modify the dynamical ages of the galaxies and alter any trend in accreted fraction with age.

The trend of accreted fraction with stellar mass is sensitive to the excess of massive galaxies in the simulations. If we restrict the sample to galaxies with  $M_* < 10^{11}$ , the slope of accreted fraction with mass is consistent with zero. Furthermore, overmerging will modify the slope of this relation. If the *real* relation between  $\log M_*$  and the accreted mass fraction, has a small or negative slope, then additional merging will tend to increase the slope; if the real slope is very steep, then overmerging will tend to flatten the slope. The value for which the slope remains unchanged is  $\sim 0.09$ , and depends only weakly on the stellar mass and average merger ratio. This value is close to the slope we measure slope, and suggests the slope in Figure 4 may be an artifact of overmerging, and the real slope could be either shallower or steeper.

Direct comparisons of the merged fraction with observations is difficult. Although there are many studies of the merger rate as a function of redshift (e.g. Le Fèvre et al. 2000; Bundy et al. 2004; Lin et al. 2004; Kartaltepe et al. 2007; Lotz et al. 2008; Jogee et al. 2009; Bridge et al. 2010, see Lotz et al. 2011 and references therein), these studies suffer from many observational biases, including difficulty in selecting comparable descendant/progenitor populations. Nonetheless, studies of paired galaxies indicate a weak positive trend in the major merger rate with progenitor galaxy mass (Bundy et al. 2009; Darg et al. 2010, but see Bridge et al. 2010). This is compatible with our results of an increase in the accreted fraction with stellar mass, provided that the average merger ratio does not decrease precipitously with galaxy mass.

### 3.1 Comparison to Oser, et al. 2010

The upper and lower panels in Figure 4 show the accreted fraction of stars for the galaxies in this work and in Os10, respectively. Both studies find the same sign for the relationship between accreted fraction and total stellar mass, but Os10 find an accreted fraction about twice as large as that found in this work. Furthermore, the slope of the Os10 relation is about twice as steep (although the mass range of their sample is smaller). We suggest that these differences in accreted fraction can be explained by several major differences in the simulations in the resolutions, the feedback models, and the star formation efficiencies.

As shown in Figure 5, even the most massive galaxies in our work experience significant late star formation. The median  $z = 0$  SFR for galaxies with stellar masses above  $10^{11} M_\odot$  is  $5.2 M_\odot \text{yr}^{-1}$ , above the observed star formation rate for most present-day massive galaxies. This ongoing star formation contributes significantly to the in-situ fraction of stars. Naab et al. (2007) have shown that higher resolution can decrease the amount of late time star formation (see their Figure 2). For the lower resolution simulations, the  $z = 0$  SFR is  $\sim 5 M_\odot \text{yr}^{-1}$ . For smoothed particle hydrodynamics (SPH) codes, like the GADGET code used in Naab et al. (2007) and Os10, the low resolution suppresses the Kelvin-Helmholtz instability (Agertz et al. 2007), which breaks up clumps of cold gas before they sink to the center of a galaxy and form in-situ stars. At higher resolutions ( $m_* < 10^5 M_\odot$ ), the final star formation rates is less than  $1 M_\odot/\text{yr}$ , even without AGN or Type I supernovae feedback (Johansson et al. 2012).

Although the AMR code used in this work does not suffer from the same problem as SPH codes at low resolution, low resolution AMR simulations will suppress fragmentation of infalling gas clouds. These gas clouds will survive to the center of the nascent galaxy, where they will form stars in-situ at late times. The high resolution simulations of Os10 use particle masses of  $m_{*, \text{gas}} = 6.0 \times 10^6 M_\odot$  and  $m_{\text{dark}} = 3.6 \times 10^7 M_\odot$ . Although not the highest mass resolution tested in Naab et al. (2007), this particle resolution is large enough to suppress most spurious late star formation. Furthermore, the simulation in Os10 have a factor 3 more mass resolution in dark matter than the simulations examined in this work. Thus, we expect additional late in-situ star formation in our simulations, and, therefore, a lower accreted fraction when compared to the simulations of Os10. Cen (2012) have performed spatial resolution tests for the cluster box and find that the overall convergence is quite good. However, they find that the metallicity in damped Lyman-alpha systems increases by around 0.2 dex for an AMR simulation with spatial resolution better by a factor of two. Therefore, we expect that improved spatial resolution will alter the star formation and feedback processes, changing the in-situ and accreted fractions. The same is certainly true for improved mass resolution, which will be tested in future work.

Both the simulations presented here and those in Os10 suffer from an overabundance of star formation, and a deficit of feedback. The differences in the feedback and cooling models may help explain the difference in accreted fraction between the two simulations. Scannapieco et al. (2011) show that the addition of metal-line cooling to GADGET3 (used by

Os10) can help decrease the final stellar mass of galaxies by  $\sim 30\%$ , but does little to the star formation history. Therefore, we expect additional cooling will have little effect on the fraction of accreted stars. However, Scannapieco et al. (2011) show that different feedback models can greatly affect the star formation history in simulations. For various models of feedback and cooling in SPH simulations, Scannapieco et al. (2011) find that the redshift by which half of the stars have formed ranges from  $\sim 1.5 - 4.0$ , comparable to the redshift range of the median stellar age from Os10. Additional supernovae feedback, especially the addition of supernovae winds, tends to decrease the median redshift of star formation. We expect that decreased early star formation will decrease the accreted fraction, as fewer small systems will form stars at high redshift to be accreted later.

In the work presented here, star formation occurs much later than in the work of Os10; Figure 5 shows half the stars in our simulations are only formed by  $z \approx 1$ , in agreement with results from other AMR codes (Scannapieco et al. 2011). As mentioned above, late star formation will lead to an increased in-situ fraction in massive galaxies. We expect that additional feedback will decrease star formation at late times and shift the median redshift of star formation to higher  $z$ . This will tend to decrease the in-situ fraction. Thus, improved feedback should bring our results and those of Os10 into better agreement.

In addition to differences in resolution and feedback, differences in star formation efficiency between the two sets of simulations affect the fraction in-situ versus accreted stars. Naab et al. (2007) have shown that the *total* stellar mass is not sensitive to the star formation timescale. However, in simulations with short star formation timescales, stars will form in small clumps outside the galaxy and will be later accreted, while in galaxies with longer star formation times, small clumps will instead be accreted as gas and later form stars in-situ. Thus, the total number of baryons accreted by the galaxy remains the same, but whether the baryons are accreted as stars or gas depends strongly on the star formation timescale. This effect is at least comparable to the effects from feedback on the accreted fraction. In comparing two grid-based codes with different star formation efficiencies, the redshift by which half the stars have formed moves from  $z \sim 2$  for an efficiency of 5% to  $z \sim 1$  for an efficiency of 1% (Scannapieco et al. 2011), comparable to the change in the median redshift of star formation from different feedback models.

Ignoring the return of mass to the gas phase from high-mass stars, the star formation rate can be written as

$$\frac{dM_*}{dt} = C_* \frac{M_{\text{gas}}}{t_{\text{dyn}}}, \quad (2)$$

where  $t_{\text{dyn}}$  is the dynamical time of the gas forming stars (see equation 1). Thus,  $1/C_* \times t_{\text{dyn}}$  is the star formation timescale,  $t_{\text{SF}}$ . Simulations with large values for  $C_*$  have short  $t_{\text{SF}}$  and therefore make stars efficiently. In the simulations examined in this work,  $C_* = 0.03$ , in agreement with theoretical calculations (Krumholz & McKee 2005) and observations (Kennicutt 1998; Evans et al. 2009). In Os10, the value for  $C_*$  is 0.083, which means for a given density gas clump, star formation is  $\sim 2.8$  times faster in the simulations used by Os10. This difference in star formation rate

becomes especially important for small clumps of baryons being accreted onto larger galaxies.

We can compare the star formation time scale to the timescale for material to fall in from the virial radius. The infall time is given by the dynamical time of the dark matter halo,  $t_{\text{virial}} \propto 1/\sqrt{G\rho_{\text{virial}}} = 1/\sqrt{200G\rho_{\text{crit}}}$ . Thus, the ratio of the star formation time to the infall time is given by

$$\begin{aligned} t_{\text{SF}}/t_{\text{virial}} &= \frac{\sqrt{200G\rho_{\text{crit}}}}{C_*\sqrt{G\rho_{\text{gas}}}} \\ &= \frac{1}{C_*} \sqrt{\frac{300}{4\pi}} H_0 t_{\text{dyn}} \\ &= 0.05h \left( \frac{1}{C_*} \right) \left( \frac{t_{\text{dyn}}}{100 \text{ Myr}} \right). \end{aligned} \quad (3)$$

For  $t_{\text{dyn}} = 100 \text{ Myr}$ , the ratio of the star formation timescale to the infall timescale is  $0.6 h$  and  $1.7 h$  for  $C_* = 0.083$  and  $0.03$ , respectively. In the first case, an infalling clump of gas above the star formation threshold density will convert  $\sim 91\%$  of its gas to stars, while in the second case only 57% of the gas will be converted into stars, and the accreted fraction will decrease by about 40%. The difference in  $C_*$  between the two simulations partially explains the difference of a factor of 2 between the accreted fractions found in this work and Os10. It also highlights the importance of the star formation efficiency in studying the merger histories of galaxies. Unlike dark matter halos, which always undergo ‘dry’ mergers, baryons can merge either as stars or gas. The relative fraction of stars to gas can have profound effects on the observable properties of galaxies.

### 3.2 Properties of accreted and in-situ stars

In addition to examining the total contribution of in-situ and accreted stars, we can also examine the mean properties of the accreted and in-situ fractions as a function of final galaxy stellar mass. The top panels in Figures 2 and 3 show the mass-weighted stellar ages and stellar metallicities for the in-situ and accreted stars as a function of  $z = 0$  galaxy stellar mass. It is immediately evident that the accreted stars are older (by 2–2.75 Gyrs) and more metal-poor (by  $\sim 0.15$  dex) than the stars formed in-situ. Figure 5 shows distributions of stellar ages for galaxies divided into three stellar mass bins. The vertical lines show the median ages for the in-situ, accreted, and total stellar masses. Again, it is clearly evident from these figures that the accreted stars are older than the in-situ stars. The plots in this figure as well as Figures 6–9 weight all galaxies in the cluster and void boxes equally. If we weight the galaxies according to the fit to the star formation history (Cen 2011b), only the results for the lowest mass bin change, and the differences in the median values are very small. Furthermore, by dividing the galaxies into mass bins, we see in Figure 5 that there is more late-time star formation in lower mass ( $M_* \lesssim 10^{11} M_\odot$ ) than in higher mass galaxies, consistent with the results of Cen (2011b) using the same simulation presented here. Examining the trends in median stellar age for the accreted and in-situ fractions as a function of mass reproduces the trends shown in Figure 2; namely, while the in-situ and accreted stellar ages only change slightly with stellar mass, the median age of all the stars increases since the accreted fraction grows with stellar mass. Finally, the difference in stellar age



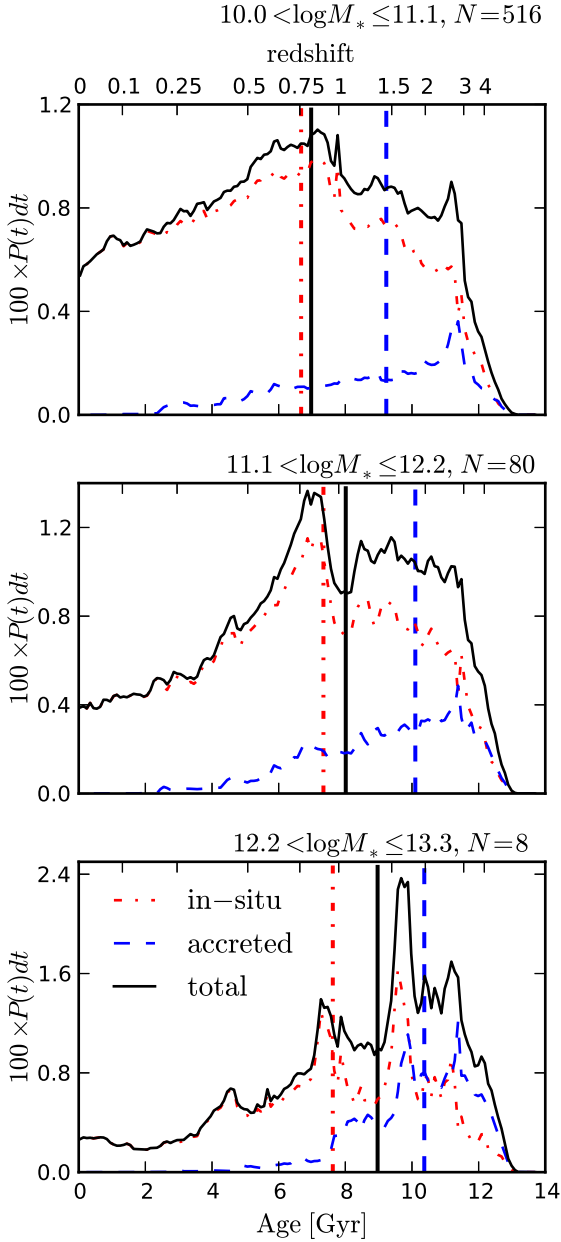


**Figure 5.** The probability distribution of stellar ages for galaxies grouped by mass. The black solid line is the total stellar age distribution. The blue dashed line is the accreted stars and the red dash-dotted line is the in-situ stars. The similar vertical lines show the median age of the stars in each category. For all mass bins, the accreted stars are  $\sim 2$  Gyrs older than the in-situ stars.

between the accreted and in-situ stars is roughly independent of total stellar mass. If we exclude galaxies more massive than  $10^{11.1} M_{\odot}$  and only examine the top panel, the accreted stars are still more than 2 Gyrs older on average than stars formed in-situ.

Since the age distributions of the in-situ and accreted stars are different, it is not surprising that the metallicity distributions are different as well (see Figure 6). For the most massive galaxies, the accreted stars are 0.12 dex more metal-poor than the stars formed in-situ. The sign of

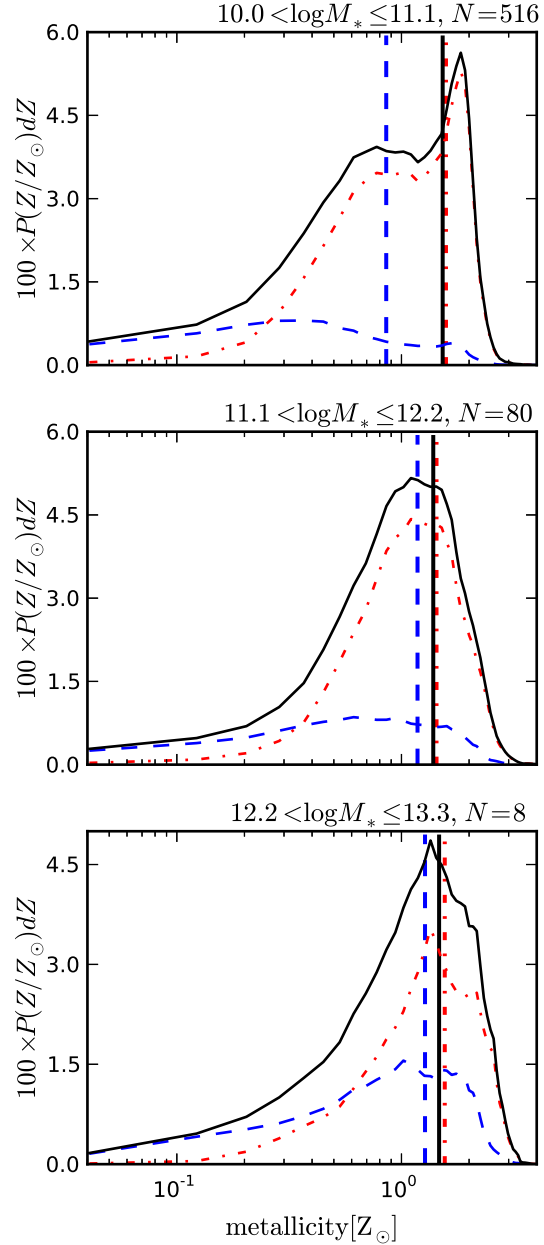


**Figure 6.** The probability distribution of stellar metallicities for galaxies grouped by mass. The lines are as in Figure 5. At all masses, the accreted stars are more metal poor than in-situ stars.

this difference is in agreement with simulation results from Font et al. (2011) for disk galaxy halos, but the metallicity difference found in this work is smaller. However, as noted above, the stellar metallicities in the simulation are sensitive to the supernovae feedback prescription, and are highly uncertain. Nonetheless, it is unlikely that improved feedback would reverse the sign of the difference in metallicity between accreted and in-situ stars. Additionally, the difference in metallicity between accreted and in-situ stars is largest for the lowest stellar mass bin, where the mass function of galaxies agrees with observations. However, additional supernovae feedback may play an important role here, as well.

The bimodal distribution of the stellar metallicities in

the low mass galaxies (see the top panel of Figure 6) may be partially due to over-weighting the cluster galaxies relative to the void galaxies. If we weight the galaxies as in Cen (2011b) (the void galaxy contribution is increased by a factor of 6), the metallicity distribution in the top panel of Figure 6 is still bimodal, but the low metallicity peak is nearly equal in height to the high metallicity peak. This remaining bimodality may be due to enhanced late star formation in metal-rich gas, which is not observed in present-day galaxies, and probably due to inadequate resolution and stellar feedback.

In addition to differences in the median stellar metallicities for accreted and in-situ stars, the dispersions are also different; the accreted stars have a larger metallicity dispersion. For the three panels in Figure 6, the inter-quartile ranges of the in-situ stellar  $Z/Z_{\odot}$  are 0.26, 0.28, and 0.27 dex. The same ranges for the accreted stars are 0.60, 0.41, and 0.34 dex. The differences in metallicity distribution width are due to the inhomogeneous make-up of the accreted material. The accreted stars are formed in a variety of systems with different metallicities, while the in-situ stars are formed in a single stellar system. The same difference in metallicity dispersion is seen in the Galactic disk and halo (e.g. Beers et al. 1985) and is used as evidence for the accretion origin of the Galactic halo (e.g. Searle & Zinn 1978; Unavane et al. 1996).

We also examine the spatial distribution of in-situ and accreted stars in galaxies at  $z = 0$ . Figure 7 shows the 3-dimensional average stellar mass profiles for the accreted and in-situ stars in three different mass bins. As expected (and as shown in the work of Oser et al. (2012)), the half-mass radius of the accreted stars is larger than the half-mass radius of the in-situ stars by approximately a factor of 2 for all three mass bins. Some of the accreted material on the outskirts of galaxies may be due to our choice of density threshold in the HOP grouping algorithm; a lower threshold will lead to larger galaxies with larger accreted fractions. In order to check how much this affects our results, we show the median radius of the stars accreted from *resolved* galaxies only in Figure 7. This radius is still larger than the median radius of the in-situ stars. Furthermore, this radius represents the minimum half-mass radius for the accreted material, as additional accretion from unresolved galaxies will tend to increase this radius.

Trends with accreted fraction and radius suggest that the average merger event is not an equal mass-merger, after which the stars would be well-mixed, but rather a minor merger in which low density material is added to the outside of a massive galaxy. It also suggests that minor mergers can substantially increase the half-light radius of massive galaxies, leading to the growth of early-type galaxies at late times. This is in agreement with both observations (Bezanson et al. 2009; van Dokkum & Brammer 2010; Newman et al. 2012; Tal et al. 2012) and other simulations (Gallagher & Ostriker 1972; Boylan-Kolchin & Ma 2004; Naab et al. 2007, 2009; Oser et al. 2012). It also follows from simple, semi-quantitative arguments based on the virial theorem (Naab et al. 2009; Bezanson et al. 2009). Because the accreted material has lower metallicity than the in-situ material, we expect galaxies to have negative metallicity and colour gradients. In projection, the average metallicity gradient for the galaxies with robust merger histories is  $d \log(Z/Z_{\odot})/d \log(R/R_{\text{eff}}) = -0.38 \pm 0.23$ , where  $R_{\text{eff}}$  is the

projected half-mass radius. Furthermore, the differences in the distributions of stellar metallicity between the accreted and in-situ stars lead to an increase in the metallicity dispersion as a function of radius. The standard deviation of  $\log Z/Z_{\odot}$  has an average slope of  $d\sigma_{\log Z/Z_{\odot}}/d \log(R/R_{\text{eff}}) = 0.28 \pm 0.18$ . There are many mechanisms besides accretion that will contribute to an increase in metallicity dispersion. Indeed, we find the in-situ stars alone also have an increase in metallicity dispersion with radius only slightly smaller than the increase reported above.

Observations of these gradients are difficult because the low surface brightness in the outskirts of galaxies. There are numerous measurements of colour gradients in early-type galaxies (de Vaucouleurs 1961; Eisenhardt et al. 2007; Tortora et al. 2010; Suh et al. 2010; Tal & van Dokkum 2011; La Barbera et al. 2011; Guo et al. 2011; Gonzalez-Perez et al. 2011), although only a few studies extend beyond the half-light radius of the galaxy. Furthermore, colour measurements cannot be used to distinguish between metallicity and age gradients. More recently, studies of the metallicity gradients of globular cluster systems in early-type galaxies support theories of two-phase galaxy formation (Arnold et al. 2011; Forbes et al. 2011). Direct measurements of metallicity gradients in the stellar populations of early type galaxies have been done using long slit spectroscopy (Davies et al. 1993; Mehlert et al. 2003; Brough et al. 2007; Spolaor et al. 2010), and integral-field-units (Rawle et al. 2008; Kuntschner et al. 2010; Greene et al. 2012). Only a few measurements focus on gradients beyond the half-light radius (Faber et al. 1977; Foster et al. 2009; Spolaor et al. 2010; Greene et al. 2012). These studies find metallicity gradients (but *not* age gradients) which indicate that accretion of low metallicity systems is important in the build-up of massive galaxies (Foster et al. 2009; Spolaor et al. 2010; Greene et al. 2012). Greene et al. (2012) find an average slope of  $[\text{Fe}/\text{H}] \approx -0.1$  from  $0 \sim 2.5 R_{\text{eff}}$  for 8 massive early type galaxies, in good agreement with the average slope we measure in the simulations. Using the iron and magnesium abundances in the outskirts of galaxies, they obtain an average mass ratio for the merger events of 10 : 1, which agrees roughly with our estimate for the mean merger ratio below (see §4.3).

Although the accreted material is made up of older stars, it is not added to the galaxies until late times. Figure 8 shows the mass-weighted average mass assembly for galaxies in three mass bins. For the central mass bin, half of the accreted stars are formed before  $z \approx 1.6$ , but it takes until  $z \approx 0.6$  for half of these stars to actually be accreted. Furthermore, Figure 8 shows that the in-situ stars are in place before the accreted material is added. The difference in assembly times between the accreted and in-situ stars is largest for the lower mass galaxies. This is consistent with the picture of two phase galaxy formation (Oser et al. 2010; Naab et al. 2007); galaxies first undergo a phase of intense, in-situ star formation, followed by a phase of accretion of old, less massive, and therefore more metal-poor systems.

### 3.3 Mergers and environment

We can also use the galaxies from the cosmological simulations to examine the properties of mergers as a function of environment. This analysis is not possible for simulations

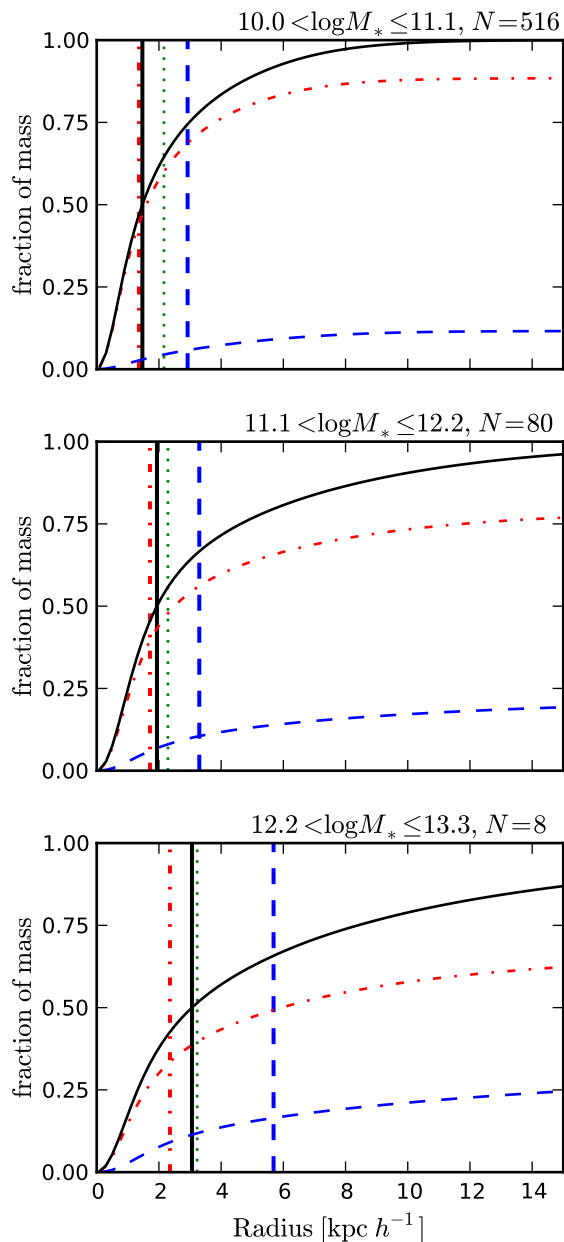


**Figure 7.** The cumulative, 3-dimensionally averaged radial stellar mass profiles for the galaxies in three mass bins. The lines are the same as in Figure 5. The vertical lines show the 3-dimensional half-mass radii for the in-situ, accreted and total stellar mass profiles. The green dotted lines show the half-mass radius for material accreted from resolved galaxies only. These represent the minimum radius for the accreted stars. The accreted stars are consistently found at larger radii than the stars formed in-situ.

which only include individual halos. Studies of paired galaxies have found a dependence on the merger rate with environment (McIntosh et al. 2008; Darg et al. 2010; Lin et al. 2010; Tonnesen & Cen 2011). This is expected, as higher density environments have more galaxies and higher potential for merging. However, part of this trend may be due to the correlation of environment and galaxy mass, which is related to the accreted fraction. By selecting a sample

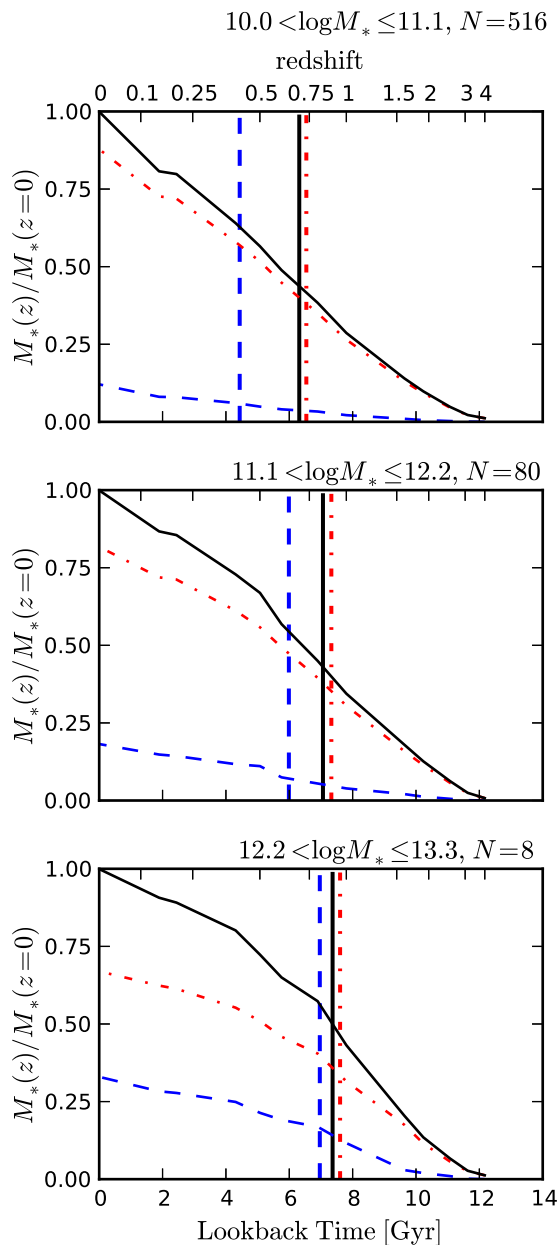


**Figure 8.** The stellar mass assembly histories for galaxies in three mass bins. The lines are the same as in Fig. 5. The vertical lines show the time at which 50% of the in-situ, accreted, and total mass is in place. While the accreted stars are typically formed at  $z \sim 1.5$ , they are assembled at  $z \sim 0.6$ .

of galaxies of similar mass, we can eliminate trends in the accreted fraction with mass and isolate the trends with environment.

We define environment as the 3-dimensional galaxy density to the 5<sup>th</sup> nearest neighbor ( $\rho_5 = 6/(\text{distance to 5}^{\text{th}} \text{ neighbor})^3 [h^3 \text{Mpc}^{-3}]$ ). The densities used are an average of the  $z = 0$  and  $z = 0.05$  measured densities in order to eliminate some of the noise introduced by the nearest neighbor density measure. We have restricted the sample to 109 galaxies with stellar masses between  $6 \times 10^{10} M_\odot < M_* < 3 \times 10^{11} M_\odot$ . Overall, we find that

the accreted fraction is not a strong function of present-day environment; the average accreted fraction increases from  $\sim 0.20$  for field galaxies to  $\sim 0.25$  for cluster galaxies. This contradicts the observations of McIntosh et al. (2008), which show an increase in the merger rate for group galaxies by a factor of 2–9 over the rate for field galaxies. The difference is due in part to our decision to study trends with environment at constant stellar mass, eliminating the larger trend. Furthermore, McIntosh et al. (2008) use group and cluster membership as a measure of environment. This measure is more sensitive to the near-field environment of a galaxy than  $\rho_5$ , and therefore, it is probably more closely correlated with the number of mergers a galaxy has undergone.

Figure 9 shows the stellar age distributions for galaxies in three density bins, which correspond to the local density for field, group, and cluster galaxies. Typical separations between galaxies in each environment bin are  $5 h^{-1}\text{Mpc}$ ,  $1 h^{-1}\text{Mpc}$ , and  $0.5 h^{-1}\text{Mpc}$ , respectively. These bins were chosen to have equal numbers of galaxies in the mass range  $6 \times 10^{10} M_\odot < M_* \leq 3 \times 10^{11} M_\odot$ . However, the results are not sensitive to the exact locations of the bin separations. As expected, the star formation histories of the galaxies in low density environments are far more extended. For field galaxies, both the in-situ and accreted stars are younger than in group and cluster galaxies by  $\sim 2$  Gyr. In fact, not only does the in-situ star formation occur later in low density regions, but the accretion also occurs  $\sim 1.5$  Gyr later than in the higher density regions. In every respect, low density regions evolve more slowly than high density regions.

Figure 10 shows the total star formation histories for galaxies in low, medium, and high density regions. These histories are normalized to the local dark matter mass in each region, which is accomplished by weighting each galaxy by the dark matter mass enclosed in a sphere centered on the galaxy and extending to the galaxy’s fifth nearest neighbor. As expected, star formation in galaxies in the lowest density environments dominates today, while, at high redshift, star formation occurred mainly in the mid- and high density regions. This is consistent with the star formation histories presented in Cen (2011b).

#### 4 ACCRETED STARS AND MERGERS

The accreted fraction of the final stellar mass is added to the galaxies through mergers. Using the simulations we can determine the rate at which mergers occur and the distribution of mass ratios of these mergers. Since the accreted fraction in most of our galaxies is less than 30% we expect that minor mergers (merger mass ratios less than 4:1) will dominate the accretion history of galaxies in our sample. In the following sections, we compute the merger rate for our sample as a function of redshift and the average merger ratios for the most massive galaxies in the simulation.

##### 4.1 Merger rates

The slopes of the in-situ and accreted mass assembly histories in Figure 8 are the star formation rates and merger rates, respectively. The star formation rate for the massive galaxies ( $\log M_*/M_\odot > 12.2$ ) peaks at  $z \approx 2.5$ , when the star

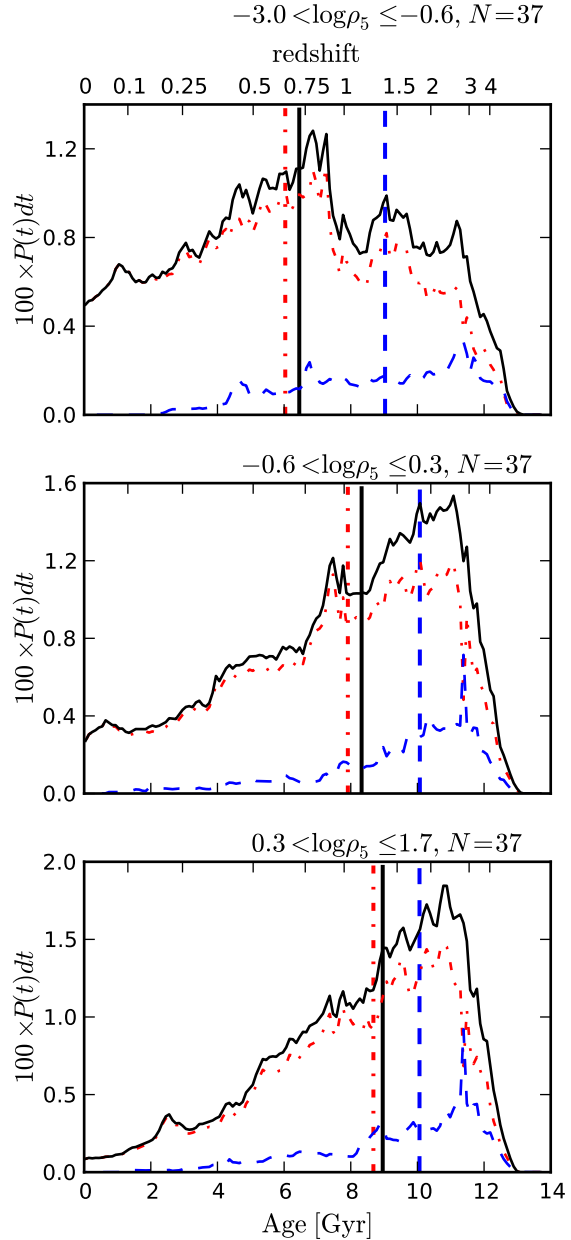


**Figure 9.** The probability distribution of stellar ages for galaxies grouped by environment ( $\rho_5$ ). The galaxies all have stellar masses between  $6 \times 10^{10} M_\odot < M_* < 3 \times 10^{11} M_\odot$ . The lines are the same as in Figure 5. Although the accreted fraction is only a weak function of environment, the median stellar age of the in-situ stars is a strong function of environment.

formation rate is high enough to double the galaxy mass within a Gyr. The accretion rate for the massive galaxies peaks later, at  $z \approx 1$ , with an average growth rate from accretion of  $\sim 15\% \text{ Gyr}^{-1}$ . At  $z = 0.25$ , the galaxies with  $M_* \gtrsim 3 \times 10^{11} M_\odot$  are adding stellar mass in mergers at a rate of  $\sim 2.6\% \text{ Gyr}^{-1}$ . This includes growth from unresolved mergers in the simulations.

The simulation merger rate is approximately a factor of two larger than the observed merger rate for luminous red galaxies (LRGs) of  $1.7\% h \text{ Gyr}^{-1}$ , where  $H_0 =$

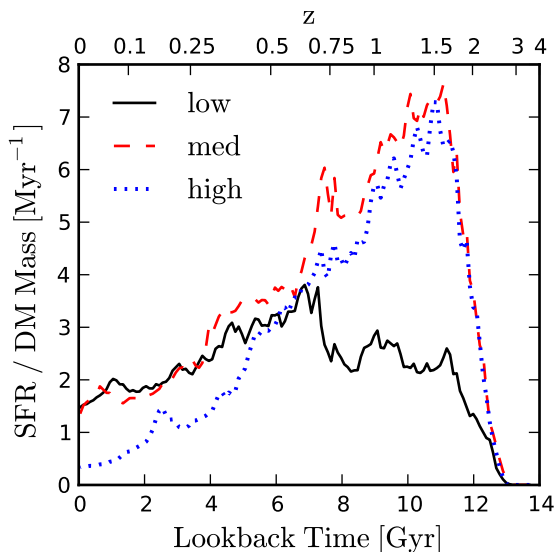


**Figure 10.** The star formation rates in different environments, for galaxies with stellar masses  $6 \times 10^{10} M_{\odot} < M_{*} < 3 \times 10^{11} M_{\odot}$  at  $z = 0$ . The different curves are normalized to the average dark matter mass associated with each galaxy, as given by 1/5 of the dark matter mass to the fifth nearest neighbor. At early times, the star formation occurs in the densest regions, while at late times the field galaxies dominate the star formation.

$100h \text{ km s}^{-1} \text{ Mpc}^{-1}$ , found by Masjedi et al. (2008) using the small scale cross correlation function to determine the close pair fraction in SDSS. This observed rate includes growth from minor mergers since the maximum luminosity ratio between the LRGs and other galaxies is  $\sim 50:1$  in SDSS observations (Masjedi et al. 2008). Since the massive galaxies in the simulation suffer from overmerging, we expect the simulation merger rate to be inflated compared to the real value.

Comparing our simulated merger rates to other observed merger rates based on paired galaxies or morphologically-disturbed galaxies is not straightforward; it requires knowing the average merger mass ratio and the merger rate of a single population of galaxies as a function of time. Assuming an average merger mass ratio between 0.15 and 0.3 (compatible with our results from §4.3), the merger rate as measured by quantified morphological disturbances ( $G - M_{20}$ ) in Lotz et al. (2011) is  $7.5 - 15\% \text{ Gyr}^{-1}$  at  $z = 0.2$  for galaxies at number densities above  $\sim 6 \times 10^{-3} \text{ Mpc}^{-3}$ . This is considerably larger than both the merger rate measured in our simulations and that measured by Masjedi et al. (2008), suggesting that the observational merger rate is still uncertain. Using higher resolution simulations with the same initial conditions, Cen (2011d) find that the observationally-defined merger rate from close pairs of galaxies does exceed the physical merger rate for simulated galaxies. This over-estimate is at least partially corrected for by including an observable timescale for the merger (Lotz et al. 2011). Despite this correction, the observed merger rates are still large. The *total* merger rate from our simulations is comparable to the observed *major* merger rates from studies of close galaxy pairs (e.g. Bundy et al. 2004; Kartaltepe et al. 2007; de Ravel et al. 2009; Bundy et al. 2009); visible dis-

turbances (tidal tail, bridges, etc.) (Jogee et al. 2009; Darg et al. 2010; Bridge et al. 2010; Kartaltepe et al. 2010), and quantified morphological disturbances (e.g. Lotz et al. 2008; Conselice et al. 2009; López-Sanjuan et al. 2009), respectively.

We can also compare the evolution of the merger rate as a function of redshift to the observations of merger rate evolution. However, care must be taken to ensure the selection of galaxies from the simulations and observations are similar. Lotz et al. (2011) argue that galaxies selected based on luminosity or mass cuts do not give the same evolution as samples selected based on constant galaxy number density, as the progenitor and descendant galaxies are different in the mass and luminosity selected samples. In our simulations, the merger rate per galaxy per Gyr for galaxies with stellar masses above  $10^{10} M_{\odot}$  grows as  $(1+z)^{2.0 \pm 0.25}$  for  $z < 1.5$ . Thus, we expect the merger rate to be an increasing function of redshift, in agreement with observations (Bridge et al. 2010, but see Bundy et al. 2009). The slope of the galaxy merger rate with redshift is similar to the slope of the dark matter merger rate with redshift (e.g. Gottlöber et al. 2001; Fakhouri & Ma 2008; Fakhouri et al. 2010). However, the simulations clearly show systems in which the dark matter halos merge well before the galaxies merge. Cosmological hydrodynamical simulations, such as those used here, can be used to measure the time lag between dark matter halo mergers and galaxies mergers, which we plan to pursue in future work.

## 4.2 Expected merger ratio

In addition to studying the rate of merging, the simulations also allow us to examine the average merger mass ratios as a function of galaxy mass. We define the merger ratio,  $\mu$ , as the mass of the accreted galaxy divided by the mass of the progenitor galaxy. By definition,  $\mu$  is always less than one. We first calculate the expected merger ratio given the galaxy mass function, and compare this expected value with the value from simulations. Similar calculations for the limiting case of small merger ratios are done in Os10 and Naab et al. (2009).

Ignoring effects of dynamical friction, gravitational focusing, and local density, the mean merger mass ratio for a galaxy is the average mass of less massive galaxies divided by the parent galaxy mass. This can be calculated from the mass function. Given a mass function  $\Phi(M)dM$ , the probability of a galaxy with mass  $M_0$  accreting a galaxy with mass in the range  $(M_a, M_a + dM)$  is

$$P(M_a)dM = \frac{\Phi(M_a)dM}{\int_{M_{\min}}^{M_0} \Phi(M)dM}, \quad (4)$$

and the number-weighted and mass-weighted average merger mass ratios are simply

$$\begin{aligned} \langle \mu_n \rangle &= \int_{M_{\min}}^{M_0} m P(m) dm / \int_{M_{\min}}^{M_0} P(m) dm, \text{ and} \\ \langle \mu_m \rangle &= \int_{M_{\min}}^{M_0} m^2 P(m) dm / \int_{M_{\min}}^{M_0} m P(m) dm, \end{aligned} \quad (5)$$

respectively. For a Schechter function,  $P(M) \propto (M/M_*)^\alpha \exp^{-M/M_*}$ , and the number-weighted and

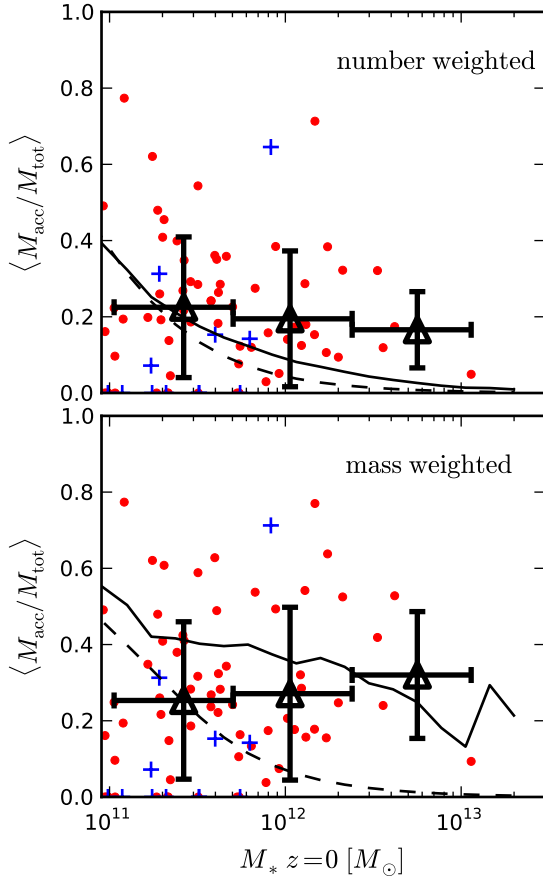


**Figure 11.** The mean merger ratios as a function of stellar mass. The red points are from the cluster box and the blue crosses are from the void box. The top panel shows the number-weighted mean merger ratio, while the bottom panel shows the mass-weighted mean merger ratio. The solid line is the expected mean merger ratio computed using the unweighted mass function from the simulation. The dotted line shows the expected mean merger ratio for a Schechter function galaxy mass distribution with  $\alpha = -1.16$  and  $\log M_* = 10.8$ .

mass-weighted average merger ratios can be evaluated as

$$\begin{aligned}
 \langle \mu_n \rangle &= 1/M_0 \times (\Gamma(\alpha + 2, M_{\min}) - \Gamma(\alpha + 2, M_0)) / \\
 &\quad (\Gamma(\alpha + 1, M_{\min}) - \Gamma(\alpha + 1, M_0)) , \\
 \langle \mu_m \rangle &= 1/M_0 \times (\Gamma(\alpha + 3, M_{\min}) - \Gamma(\alpha + 3, M_0)) / \\
 &\quad (\Gamma(\alpha + 2, M_{\min}) - \Gamma(\alpha + 2, M_0)) , \quad (6)
 \end{aligned}$$

where masses are given in units of  $M_*$ , and we have included a lower limit on the mass function,  $M_{\min}$ . The dashed lines in Figure 11 show the numerical values for  $\langle \mu_n \rangle$  and  $\langle \mu_m \rangle$  for  $\alpha = -1.16$  and  $\log M_*/M_{\odot} = 10.8$ , the Schechter function parameters fit to the SDSS sample (Li & White 2009). The integrals are stopped at and  $M_{\min} = 10^9 M_{\odot}$ . This procedure yields similar results to the expected merger mass ratio calculated by Hopkins et al. (2010) using N-body simulations for the merger trees and semi-empirical methods for determining the galaxy properties. Hopkins et al. (2010) find that  $\langle \mu_m \rangle$  peaks around  $M_* \approx 10^{11} M_{\odot}$ , and decreases for both larger and smaller galaxy masses.

### 4.3 Mean merger mass ratio

In §2.2 we show that the simulated mass function deviates from the observed mass function below  $M_* < 10^{10} M_{\odot}$ . Therefore, in this section, we only examine mergers between galaxies with stellar masses greater than  $10^{10} M_{\odot}$  at  $z < 2.5$ . We require that the final galaxy mass is larger than  $10^{11} M_{\odot}$ , thus allowing us to resolve mergers with a mass ratio of  $\mu < 0.1$  at  $z = 0$ . This limits the sample to the most massive galaxies which suffer from over-cooling and too much star formation, making comparisons to observations ineffective. This sample includes 85 galaxies from the cluster box and 15 galaxies from the void box. Figure 11 shows the mean mass-weighted and number-weighted merger ratios as a function of  $z = 0$  stellar mass. The large triangles denote median merger ratios and do not show a significant trend with galaxy mass, although the maximum merger ratio increases with decreasing stellar mass. The averages are consistent with the expected merger ratio from the mass function in the simulation (solid line). The excess of massive galaxies due to over-cooling makes the expected merger ratios in the simulation deviate from the merger ratios predicted by a Schechter function galaxy mass distribution (cf. Figure 1). The  $3\text{-}\sigma$  clipped average values for  $\langle \mu_n \rangle$  and  $\langle \mu_m \rangle$  are  $0.20 \pm 0.16$  and  $0.26 \pm 0.21$ , respectively. These results are roughly consistent with the merger ratios calculated in Hopkins et al. (2010) using semi-empirical techniques.

Oser et al. (2012) examine the average merger ratio for the same set of galaxies used in Os10. They also find little trend with merger ratios and stellar mass, but their average merger ratios are lower than the ones we find here and closer to the analytically derived values. Because the simulations in Os10 are of higher mass resolution, they are able to resolve mergers down to lower mass ratios. Therefore, it is not surprising that they find a substantially lower value for  $\langle \mu_n \rangle$ , which is affected by many low mass mergers, while their value for  $\langle \mu_m \rangle$  is comparable to the  $\langle \mu_m \rangle$  we measure. Because we are restricted to mergers with mass ratios greater than 10:1, the plots in Figure 11 only account for 75% of the accretion onto the galaxies shown. The other 25% of the accretion is from galaxies below our mass cutoff and other unresolved accretion. Accounting for this accretion sets a lower limit on  $\langle \mu_m \rangle$  of 0.20, in agreement with the results from Oser et al. (2012). Finally, the low value for  $\langle \mu_n \rangle$  reported by Oser et al. (2012) is consistent with the differences in star formation efficiency in the two works; the higher star formation efficiency in Os10 and Oser et al. (2012) should yield more small stellar systems than in our simulations, which will decrease  $\langle \mu_n \rangle$ .

## 5 DISCUSSION AND SUMMARY

The two-phase picture of galaxy formation put forward by Os10 provides a useful framework for studies of galaxy evolution. We apply this framework to study the galaxy merger histories of more than 600 simulated galaxies with  $M_* > 10^{10} M_{\odot}$ . In this work, we corroborate the two-phase model for galaxy formation. The first phase consists of a period of in-situ star formation, which occurs around  $0.75 < z < 1$ . This in-situ phase accounts for 60–90% of the star formation in galaxies with stellar masses above  $10^{10} M_{\odot}$ . The



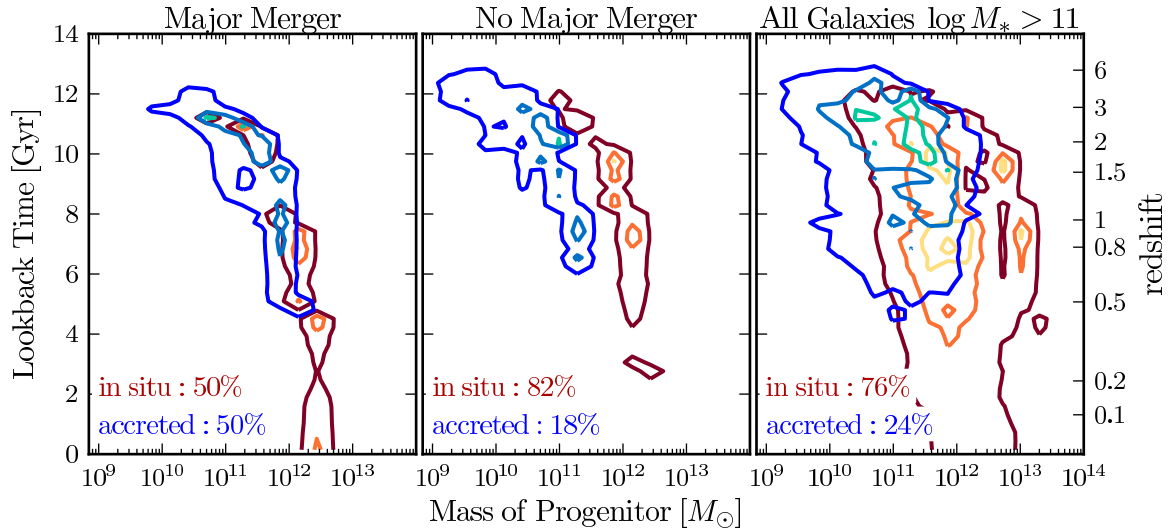


**Figure 12.** Distributions of stellar ages and host galaxy masses for accreted (blue contours) and in-situ (red contours) stars. The x-axis shows the mass of the galaxy in which a given star particle formed. The left panel shows the distribution for a galaxy which underwent a major merger at  $z \approx 0.4$ . The center panel shows a galaxy which had no major mergers. The right panel shows the distribution of stars for all massive galaxies in the simulation. The contours have been smoothed and enclose 20, 50, and 80 per cent of the stars. The differences between the accreted and in-situ stars are largest for galaxies with no major mergers.

remainder of the stars are added in mergers. The peak of the merger activity occurs at  $z \approx 0.5$ , after the majority of the in-situ star formation has taken place. Our results are in good agreement with those from Os10 and other simulations distinguishing between accreted and in-situ star formation in stellar halos, mainly around disk galaxies (e.g. Font et al. 2011; Abadi et al. 2006; Zolotov et al. 2009, 2010). In particular, the differences in stellar age, metallicity, and spatial distribution shown in Figures 5–7 are in agreement with the differences found by Font et al. (2011) and Zolotov et al. (2009).

Although the accretion occurs at late times, the accreted systems are old. The accreted stars are on average 2 Gyr older than the stars formed in-situ. This age difference correlates with a median metallicity difference of 0.15 dex. Since the accreted material comes from a variety of sources (i.e., a range of galaxy host masses), the distribution of stellar metallicities is larger for the accreted stars than for the in-situ stars. However, the simulated galaxies do not conform to the mass-metallicity relation, suggesting that the stellar feedback model does not provide sufficient feedback, and that higher resolution is needed. Improved feedback prescriptions should lower the stellar metallicities for the less massive galaxies and the accreted systems, thus increasing the differences in metallicity between in-situ and accreted stars. This effect may be countered by a decrease in metallicity in the centers of galaxies, if higher resolution and better feedback prescription help shut off the excess late star formation currently seen in the simulations.

Unlike in simulations, observations cannot easily distinguish between stars formed in-situ and those added by accretion. Nonetheless, we find indirect signs of the two phases of galaxy formation which are observable today. Because the accreted stars formed in small systems at early times, their stellar ages and metallicities are noticeably different from

the stars formed in-situ. Furthermore, because the accreted stars preferentially reside in the outskirts of galaxies, we find strong gradients in the stellar populations of massive galaxies which have been observed beyond the half light radius of early-type galaxies (Foster et al. 2009; Spolaor et al. 2010; Greene et al. 2012).

As explained above, our results are consistent with models of hierarchical formation of galaxies; large systems are assembled at late times from older, smaller building blocks. Figure 12 is an illustration of the hierarchical growth. Here, we plot the stellar age against the stellar mass of the system (galaxy) in which each star was born, for the accreted and in-situ stars, separately. For a galaxy with no major mergers (central panel), the distribution of accreted and in-situ stars are well separated. On average, accreted stars form early in small systems, while in-situ star formation occurs later, when the host galaxy is more massive. On the other hand, the distributions of accreted and in-situ stars are very similar for a galaxy which underwent a major merger (left panel). This is unsurprising since two galaxies with roughly the same mass should have similar star formation histories.

The overall trends in Figure 12 suggest that galaxy stellar mass and stellar age are anti-correlated. However, the low mass galaxies shown in this figure formed early and were subsequently accreted, at which point they stopped forming stars. These galaxies are not representative of present-day low mass galaxies, but are rather the building blocks of more massive galaxies. Indeed, the top panel of Figure 2 shows stellar mass and stellar age are correlated for galaxies which survive to  $z = 0$ , in qualitative agreement with observations.

Observations cannot directly reproduce Figure 12. However, there may be a close mapping from the relation between stellar ages and progenitor masses to the relation between metallicity and  $\alpha$ -element enhancement

(Thomas et al. 2005; Johnston et al. 2008). Old stellar populations have higher alpha-to-iron abundance ratios than younger stellar systems, while massive galaxies typically have higher metallicities than less massive systems. Figure 12 shows that accreted stars come from older, less massive systems, so we expect that accreted stars should be alpha-element enhanced compared to stars formed in-situ. This will yield radial gradients in abundance ratios in addition to the gradients in metallicity discussed above. This stellar abundance space is used to map the accretion history of the Galactic halo (Bland-Hawthorn & Freeman 2003; Robertson et al. 2005; Font et al. 2006b,a; Johnston et al. 2008; Zolotov et al. 2010). Using simulations of a Milky Way analogue, Tissera et al. (2012) find that the accreted stars in the disc (15% of the disc stars) are alpha-enhanced and older than the stars formed in-situ, in broad agreement with our results shown in Figure 12. This type of analysis is being extended to galaxies besides the Milky Way by measuring  $\alpha$ -to-Fe ratios as a function of galaxy radius (Kuntschner et al. 2010; Spolaor et al. 2010; Greene et al. 2012). As detailed chemical and spatial information becomes available for the outer regions of more galaxies, it may be possible to differentiate between a minor merger and major merger driven galaxy formation history for individual galaxies.

The results of this work agree broadly with the results of Os10 based on a set of 40 galaxies simulated using GADGET, an SPH code, at higher mass resolution. We claim that most of the differences can be accounted for by the differences in star formation efficiency, feedback, and resolution between the simulations. The higher star formation efficiency in Os10 yields a higher accreted fraction because small halos have time to form stars during infall from the virial radius of larger halos. These small stellar systems tend to decrease the number-weighted mean merger ratio (Oser et al. 2012). In our simulations, the lower resolution tends to increase the in-situ star formation rate by preventing gas clumps from fragmenting and forming stars before being accreted. These gas clumps survive to the centers of the galaxies, where they then form stars in-situ. The effects of resolution on the in-situ and accreted fractions will be checked in future AMR simulations run at higher resolution. Together with the differences in feedback, these effects account for the difference of a factor of two between the accreted fraction observed in the SPH and AMR simulations. Despite these differences, there is an excellent qualitative agreement between this work and the work in Os10. This shows that the two phase model for the formation of massive galaxies is robust and independent of the numerical methods and subgrid physics. Therefore, the simulations can be used to predict observable consequences of the two phases of galaxy formation. In this work, we show that the differences in age, metallicity, and metallicity dispersion between the accreted and in-situ stars yield radial gradients in these quantities for present-day massive galaxies. Currently, there is evidence for radial trends in metallicity in early-type galaxies (cf. Greene et al. 2012; Spolaor et al. 2010), consistent with our predictions for two phase galaxy formation and further observational tests of this picture will be extremely useful.

## ACKNOWLEDGMENTS

We are very grateful to the referee whose insightful comments greatly improved this manuscript. We also thank Greg Bryan for help with Enzo code, and Ludwig Oser for useful comments and providing data for comparison. Computing resources were in part provided by the NASA High-End Computing (HEC) Program through the NASA Advanced Supercomputing (NAS) Division at Ames Research Center. This work is supported in part by grants NNX11AI23G. CNL acknowledges support from the NSF grant AST0908368.

## REFERENCES

- Abadi M. G., Navarro J. F., Steinmetz M., 2006, MNRAS, 365, 747
- Agertz O., et al. 2007, MNRAS, 380, 963
- Arnold J. A., et al. 2011, ApJ, 736, L26+
- Beers T. C., Preston G. W., Shectman S. A., 1985, AJ, 90, 2089
- Behroozi P. S., Conroy C., Wechsler R. H., 2010, ApJ, 717, 379
- Bezanson R., van Dokkum P. G., Tal T., Marchesini D., Kriek M., Franx M., Coppi P., 2009, ApJ, 697, 1290
- Bland-Hawthorn J., Freeman K. C., 2003, in E. Perez, R. M. Gonzalez Delgado, & G. Tenorio-Tagle ed., Star Formation Through Time Vol. 297 of Astronomical Society of the Pacific Conference Series, Unravelling the Epoch of Dissipation. p. 457
- Blanton M. R., et al. 2003, ApJ, 592, 819
- Boylan-Kolchin M., Ma C., 2004, MNRAS, 349, 1117
- Bridge C. R., Carlberg R. G., Sullivan M., 2010, ApJ, 709, 1067
- Brook C. B., Kawata D., Gibson B. K., Flynn C., 2004, MNRAS, 349, 52
- Brough S., Proctor R., Forbes D. A., Couch W. J., Collins C. A., Burke D. J., Mann R. G., 2007, MNRAS, 378, 1507
- Bruzual G., Charlot S., 2003, MNRAS, 344, 1000
- Bryan G. L., 1999, Comput. Sci. Eng., Vol. 1, No. 2, p. 46 - 53, 1, 46
- Bundy K., Fukugita M., Ellis R. S., Kodama T., Conselice C. J., 2004, ApJ, 601, L123
- Bundy K., Fukugita M., Ellis R. S., Targett T. A., Belli S., Kodama T., 2009, ApJ, 697, 1369
- Carlberg R. G., 1984, ApJ, 286, 416
- Carrasco E. R., Conselice C. J., Trujillo I., 2010, MNRAS, 405, 2253
- Cen R., 2011a, ArXiv e-prints
- Cen R., 2011b, ApJ, 741, 99
- Cen R., 2011c, ApJ, 742, L33
- Cen R., 2011d, ArXiv e-prints
- Cen R., 2012, ApJ, 748, 121
- Cen R., Kang H., Ostriker J. P., Ryu D., 1995, ApJ, 451, 436
- Cen R., Nagamine K., Ostriker J. P., 2005, ApJ, 635, 86
- Cen R., Ostriker J. P., 1992, ApJ, 399, L113
- Ceverino D., Dekel A., Bournaud F., 2010, MNRAS, 404, 2151
- Coccato L., Gerhard O., Arnaboldi M., Ventimiglia G., 2011, A&A, 533, A138



- Conselice C. J., Yang C., Bluck A. F. L., 2009, MNRAS, 394, 1956
- Crain R. A., et al. 2009, MNRAS, 399, 1773
- Croton D. J., et al. 2006, MNRAS, 365, 11
- Daddi E., et al. 2005, ApJ, 626, 680
- Damjanov I., et al. 2009, ApJ, 695, 101
- Darg D. W., et al. 2010, MNRAS, 401, 1552
- Davies R. L., Sadler E. M., Peletier R. F., 1993, MNRAS, 262, 650
- de Ravel L., Le Fèvre O., Tresse L., Bottini D., Garilli B., Le Brun V., Maccagni D., Scaramella R., Scodreggio M., Vettolani G., Zanichelli A., Adami C., Arnouts S., et al., 2009, A&A, 498, 379
- de Vaucouleurs G., 1961, ApJS, 5, 233
- Deason A. J., Belokurov V., Evans N. W., 2011, MNRAS, 411, 1480
- Dekel A., Birnboim Y., 2006, MNRAS, 368, 2
- Dekel A., Sari R., Ceverino D., 2009, ApJ, 703, 785
- Eggen O. J., Lynden-Bell D., Sandage A. R., 1962, ApJ, 136, 748
- Eisenhardt P. R., De Propriis R., Gonzalez A. H., Stanford S. A., Wang M., Dickinson M., 2007, ApJS, 169, 225
- Eisenstein D. J., Hu W., 1999, ApJ, 511, 5
- Elmegreen B. G., Elmegreen D. M., Fernandez M. X., Lemonias J. J., 2009, ApJ, 692, 12
- Evans II N. J., et al. 2009, ApJS, 181, 321
- Faber S. M., Burstein D., Dressler A., 1977, AJ, 82, 941
- Fakhouri O., Ma C.-P., 2008, MNRAS, 386, 577
- Fakhouri O., Ma C.-P., Boylan-Kolchin M., 2010, MNRAS, 406, 2267
- Font A. S., Johnston K. V., Bullock J. S., Robertson B. E., 2006a, ApJ, 638, 585
- Font A. S., Johnston K. V., Bullock J. S., Robertson B. E., 2006b, ApJ, 646, 886
- Font A. S., McCarthy I. G., Crain R. A., Theuns T., Schaye J., Wiersma R. P. C., Dalla Vecchia C., 2011, MNRAS, 416, 2802
- Forbes D. A., Spitler L. R., Strader J., Romanowsky A. J., Brodie J. P., Foster C., 2011, MNRAS, 413, 2943
- Foster C., Proctor R. N., Forbes D. A., Spolaor M., Hopkins P. F., Brodie J. P., 2009, MNRAS, 400, 2135
- Fukugita M., Ichikawa T., Gunn J. E., Doi M., Shimasaku K., Schneider D. P., 1996, AJ, 111, 1748
- Fukugita M., Peebles P. J. E., 2004, ApJ, 616, 643
- Gallagher III J. S., Ostriker J. P., 1972, AJ, 77, 288
- Gallazzi A., Brinchmann J., Charlot S., White S. D. M., 2008, MNRAS, 383, 1439
- Gallazzi A., Charlot S., Brinchmann J., White S. D. M., Tremonti C. A., 2005, MNRAS, 362, 41
- Gonzalez-Perez V., Castander F. J., Kauffmann G., 2011, MNRAS, 411, 1151
- Gottlöber S., Klypin A., Kravtsov A. V., 2001, ApJ, 546, 223
- Greene J. E., Murphy J. D., Comerford J. M., Gebhardt K., Adams J. J., 2012, ArXiv e-prints
- Guo Q., White S., Li C., Boylan-Kolchin M., 2010, MNRAS, 404, 1111
- Guo Y., et al. 2011, ApJ, 735, 18
- Haardt F., Madau P., 1996, ApJ, 461, 20
- Hopkins P. F., et al. 2010, ApJ, 715, 202
- Hopkins P. F., Bundy K., Murray N., Quataert E., Lauer T. R., Ma C.-P., 2009, MNRAS, 398, 898
- Jogee S., et al. 2009, ApJ, 697, 1971
- Johansson P. H., Naab T., Ostriker J. P., 2012, ArXiv e-prints
- Johnston K. V., Bullock J. S., Sharma S., Font A., Robertson B. E., Leitner S. N., 2008, ApJ, 689, 936
- Joung M. R., Cen R., Bryan G. L., 2009, ApJ, 692, L1
- Kartaltepe J. S., et al. 2010, ApJ, 721, 98
- Kartaltepe J. S., et al. 2007, ApJS, 172, 320
- Kauffmann G., White S. D. M., Guiderdoni B., 1993, MNRAS, 264, 201
- Kennicutt Jr. R. C., 1998, ApJ, 498, 541
- Komatsu E., et al. 2011, ApJS, 192, 18
- Krumholz M. R., McKee C. F., 2005, ApJ, 630, 250
- Kuntschner H., et al. 2010, MNRAS, 408, 97
- La Barbera F., Ferreras I., de Carvalho R. R., Lopes P. A. A., Pasquali A., de la Rosa I. G., De Lucia G., 2011, ApJ, 740, L41
- Larson R. B., 1975, MNRAS, 173, 671
- Le Fèvre O., et al. 2000, MNRAS, 311, 565
- Leauthaud A., et al. 2012, ApJ, 746, 95
- Li C., White S. D. M., 2009, MNRAS, 398, 2177
- Lin L., et al. 2010, ApJ, 718, 1158
- Lin L., et al. 2004, ApJ, 617, L9
- López-Sanjuan C., Balcells M., Pérez-González P. G., Barro G., García-Dabó C. E., Gallejo J., Zamorano J., 2009, A&A, 501, 505
- Lotz J. M., et al. 2008, ApJ, 672, 177
- Lotz J. M., Jonsson P., Cox T. J., Croton D., Primack J. R., Somerville R. S., Stewart K., 2011, ApJ, 742, 103
- Masjedi M., Hogg D. W., Blanton M. R., 2008, ApJ, 679, 260
- McIntosh D. H., Guo Y., Hertzberg J., Katz N., Mo H. J., van den Bosch F. C., Yang X., 2008, MNRAS, 388, 1537
- Mehlert D., Thomas D., Saglia R. P., Bender R., Wegner G., 2003, A&A, 407, 423
- Moore B., Katz N., Lake G., 1996, ApJ, 457, 455
- Moster B. P., Somerville R. S., Maulbetsch C., van den Bosch F. C., Macciò A. V., Naab T., Oser L., 2010, ApJ, 710, 903
- Naab T., Johansson P. H., Ostriker J. P., 2009, ApJ, 699, L178
- Naab T., Johansson P. H., Ostriker J. P., Efstathiou G., 2007, ApJ, 658, 710
- Newman A. B., Ellis R. S., Bundy K., Treu T., 2012, ApJ, 746, 162
- Nissen P. E., Schuster W. J., 2010, A&A, 511, L10
- Oser L., Naab T., Ostriker J. P., Johansson P. H., 2012, ApJ, 744, 63
- Oser L., Ostriker J. P., Naab T., Johansson P. H., Burkert A., 2010, ApJ, 725, 2312
- O'Shea B. W., Bryan G., Bordner J., Norman M. L., Abel T., Harkness R., Kritsuk A., 2004, ArXiv Astrophysics e-prints
- Ostriker J. P., Hausman M. A., 1977, ApJ, 217, L125
- Peebles P. J. E., 2001, ApJ, 557, 495
- Rawle T. D., Smith R. J., Lucey J. R., Swinbank A. M., 2008, MNRAS, 389, 1891
- Raymond J. C., Cox D. P., Smith B. W., 1976, ApJ, 204, 290
- Robertson B., Bullock J. S., Font A. S., Johnston K. V., Hernquist L., 2005, ApJ, 632, 872
- Scannapieco C., et al. 2011, ArXiv e-prints

- Searle L., Zinn R., 1978, *ApJ*, 225, 357  
 Spinrad H., Taylor B. J., 1971, *ApJS*, 22, 445  
 Spolaor M., et al., 2010, *MNRAS*, 408, 272  
 Springel V., et al. 2005, *Nat*, 435, 629  
 Suh H., Jeong H., Oh K., Yi S. K., Ferreras I., Schawinski K., 2010, *ApJS*, 187, 374  
 Tal T., van Dokkum P. G., 2011, *ApJ*, 731, 89  
 Tal T., Wake D. A., van Dokkum P. G., van den Bosch F. C., Schneider D. P., Brinkmann J., Weaver B. A., 2012, *ApJ*, 746, 138  
 Thomas D., Maraston C., Bender R., Mendes de Oliveira C., 2005, *ApJ*, 621, 673  
 Tissera P. B., White S. D. M., Scannapieco C., 2012, *MNRAS*, 420, 255  
 Tonnesen S., Cen R., 2011, *ArXiv e-prints*  
 Tortora C., Napolitano N. R., Cardone V. F., Capaccioli M., Jetzer P., Molinaro R., 2010, *MNRAS*, 407, 144  
 Trujillo I., Conselice C. J., Bundy K., Cooper M. C., Eisenhardt P., Ellis R. S., 2007, *MNRAS*, 382, 109  
 Unavane M., Wyse R. F. G., Gilmore G., 1996, *MNRAS*, 278, 727  
 van de Sande J., Kriek M., Franx M., van Dokkum P. G., Bezanson R., Whitaker K. E., Brammer G., Labbé I., Groot P. J., Kaper L., 2011, *ApJ*, 736, L9  
 van der Wel A., Holden B. P., Zirm A. W., Franx M., Retura A., Illingworth G. D., Ford H. C., 2008, *ApJ*, 688, 48  
 van der Wel A., Rix H.-W., Wuyts S., McGrath E. J., Koekemoer A. M., Bell E. F., Holden B. P., Robaina A. R., McIntosh D. H., 2011, *ApJ*, 730, 38  
 van Dokkum P. G., Brammer G., 2010, *ApJ*, 718, L73  
 van Dokkum P. G., Franx M., Kriek M., Holden B., Illingworth G. D., Magee D., Bouwens R., Marchesini D., Quadri R., Rudnick G., Taylor E. N., Toft S., 2008, *ApJ*, 677, L5  
 White S. D. M., 1976, *MNRAS*, 177, 717  
 White S. D. M., Rees M. J., 1978, *MNRAS*, 183, 341  
 Wiersma R. P. C., Schaye J., Theuns T., 2011, *MNRAS*, 415, 353  
 Woodward P., Colella P., 1984, *Journal of Computational Physics*, 54, 115  
 Zolotov A., et al. 2009, *ApJ*, 702, 1058  
 Zolotov A., Willman B., Brooks A. M., Governato F., Hogg D. W., Shen S., Wadsley J., 2010, *ApJ*, 721, 738